Heliyon 9 (2023) e18959

Contents lists available at ScienceDirect

Heliyon

journal homepage: www.cell.com/heliyon

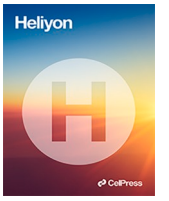

P92 steel and inconel 617 alloy welds joint produced using ERNiCr-3 filler with GTAW process: Solidification mechanism, microstructure, mechanical properties and residual stresses

Amit Kumar [a], Shailesh M. Pandey [b], Sachin Sirohi [c,**], Dariusz Fydrych [d,***], Chandan Pandey [a,*]

[a] Department of Mechanical Engineering, IIT Jodhpur, Jodhpur, 342037, India
[b] Department of Mechanical Engineering, NIT Patna, Patna, 201204, India
[c] Department of Mechanical Engineering, SRM Institute of Science and Technology, Delhi NCR Campus, Modinagar 201204, Uttar Pradesh, India
[d] Institute of Manufacturing and Materials Technology, Faculty of Mechanical Engineering and Ship Technology, Gdańsk University of Technology, Gdańsk 80-233, Poland

ARTICLE INFO

Keywords:
Dissimilar welded joint
Groove geometry
ERNiCr-3 filler
Characterization
Mechanical testing
Residual stresses

ABSTRACT

The objective of the current study was to analyse the microstructure, mechanical characteristics, and residual stresses of a dissimilar welded joint (DWJ) made of P92 steel and the Inconel alloy 617 (IN617) using the gas tungsten arc welding (GTAW) method. The ERNiCr-3 filler was selected to produce the conventional V groove (VG) and narrow V groove (NVG) butt joint. The filler deficient zones in the weldments, such as the filler deficient beach, i.e. unmixed zone (UZ), peninsula, and island, as well as the distinct heat-affected zone (HAZ), were visible near the interface of ERNiCr-3 filler weld and P92 steel due to the distinct differences in the chemical composition, microstructure, and mechanical properties between the filler and P92 base metal (BM). A very narrow partial melted zone (PMZ) and almost negligible UZ and HAZ were noticed at the interface of IN617 and ERNiCr-3 weld metal and it occurred mainly due to the similarity in microstructure and melting point. The austenitic microstructure of ERNiCr-3 filler weld was accompanied by precipitates enriched with Ti and Nb along with the inter-dendritic space. At room temperature, the mechanical properties of both the groove joints were evaluated, and the test results indicated that the welded joint satisfied the standard requirements for AUSC power plants' boiler applications. The tensile test results showed the failure from ERNiCr-3 filler weld with a tensile strength of 627 ± 2 MPa and 636 ± 3 MPa for VG and NVG welded joints, respectively. A poor weld metal impact toughness in comparison to the BMs was attributed to the presence of the brittle Ti(C, N) and Nb(C) particles in the interdendritic space. The impact toughness for the NVG weld joint was measured higher than for the VG weld joint. A significant hardness deviation was measured along the weldments that might be due to heterogeneous microstructure, i.e. UZ, HAZ, delta ferrite, and weld metal. To impart the ductility and temper the martensite in P92 HAZ, post-weld heat treatment (PWHT) was also performed, and a studied their effect on microstructure evolution across the weldments and mechanical properties. Groove

* Corresponding author.
** Corresponding author.
*** Corresponding author.
E-mail addresses: sachinsirohi2008@gmail.com (S. Sirohi), darfydry@pg.edu.pl (D. Fydrych), chandanpy.1989@gmail.com, jscpandey@iitj.ac.in (C. Pandey).

https://doi.org/10.1016/j.heliyon.2023.e18959
Received 7 March 2023; Received in revised form 12 July 2023; Accepted 3 August 2023
Available online 7 August 2023

design also showed a significant effect on residual stress variation. The work highlights the groove geometry, welding procedure, evolution of the microstructure along the weldments, mechanical characteristics, and residual stress variation of DWJ of P92 steel and IN617 alloy. In comparison to conventional VG joints, the NVG joints exhibited superior mechanical properties and lower residual stress values.

1. Introduction

Over the years, interest in dissimilar metal welds of steel and Inconel alloys has increased because of their application in Advanced Ultra Super Critical (AUSC) power units operated at a temperature above 700 °C and pressure of 300–350 bar [1,2]. Ni-based superalloys like Alloy617, Alloy625, and Alloy740 have been considered the candidate material in AUSC power plants for components that operate at a temperature of more than 700 °C [3] because of their excellent oxidation resistance, corrosion resistance, and creep strength. However, the presence of strengthening elements Ni, Cr, Co, Mo, and Nb makes these alloys more expensive as compared to conventionally used Fe-alloy [4]. Thus in replacement of Ni-based superalloy, less expensive ferritic/martensitic Cr–Mo steels are used for components operating below 620 °C and it offers excellent creep and fatigue strength at elevated service temperature [5,6]. P92 steel, the most advanced member of the Cr–Mo steel family, was formulated by changing the composition of P91 steel, adding 1.8% W and 0.002%B, and it offers a low coefficient of thermal expansion (CTE) and high thermal conductivity as compared to other members of this family and austenitic grade steel [7,8]. Hence to achieve better flexibility in design and application, save the novel expensive Ni-based material, and compromise the operating temperature limits of P92 steel, a transition joint between Ni-based alloy and P92 steel becomes the prime interest of many researchers [9]. However, joining two metal alloys of different chemical compositions, microstructure, melting points, and CTE is a challenging task [10]. The thermal stresses generated during the welding of dissimilar materials because of the frequent thermal cycle may be the cause of failure [11]. The major issue faced in dissimilar joining is the finding of the correct filler metal having mechanical properties and thermos-physical properties between two base metals (BM). Ni-based Inconel fillers are recommended as the appropriate filler to make a DWJ, as its CTE falls between P92 steel and IN617 [12].

As compared to austenitic filler, Inconel filler enhances the creep strength and mechanical properties by retarding the carbon diffusion from steel to filler metal and also reduces the tendency of hot cracking [13]. The Inconel filler (ERNiCr-3 and ERNiCrMo-3) shows the poor solubility of carbon and hence reduces the diffusion of carbon from steel to Inconel filler and also the carbon activity gradient between steel and filler [14,15]. The alloying elements Cr, Ti, Nb, and Co are added in Inconel alloy filler to enrich the performance of the welded joint however it causes precipitation of the harmful carbide phases along the inter-dendritic spaces and cracking in the weld metal which deteriorates the mechanical properties of the welded joint [16]. Mittal and Sidhu [17] studied the combined effect of the welding process and filler composition (both austenitic and Inconel filler) on the tensile properties and hardness of dissimilar weldments of T91/347H steel. The Inconel filler (ERNiCr-3) with the GTAW process showed a good combination of tensile strength and ductility. Ramkumar et al. [18] asserted that during the welding process, the strengthening elements like Cr and Mo, present in Inconel filler are likely to segregate at inter-dendritic areas of the weld metal and lead to the evolution of secondary phase particles or intermetallic phases which results in poor mechanical and creep performance as it imparts the damaging effect and introduces the heterogeneity in the microstructure of the weld metal. Vishwakarma et al. [19] reported that elements S, P, and C present in filler metal mainly induce the hot cracking in the weld metal and deteriorate the mechanical performance of the welded joint during service temperature. Another study identified the primary cause of hot cracking as the constitutional liquation between the carbide particle/Laves phase and the Ni-rich austenitic matrix [20]. Sometimes the residual stresses developed in the weld metal and at the interface as a result of multi-pass cycling or mismatch of CTE also act as a source of hot cracking [21]. The dissimilar welding has been subjected to several other issues like residual stresses variation along weldments due to mismatch in CTE, oxidation/notch formation at service temperature at the interface of steel and Inconel filler weld, carbon diffusion and failure of the components from the soft carbon depleted zone or from soft heat-affected zone [14].

Sireesha et al. [22] evaluated the effect of varying fillers (316, 16-8-2, Inconel 82, and Inconel 182) on the structural reliability of the DWJ of 316LN/Alloy 800. The best combination of the mechanical properties and higher resistance to hot cracking was obtained for Inconel 82/182 filler. The weld metal produced using the 316 filler showed poor impact energy of 45 J after ageing while the maximum of 137 J was measured for Inconel 82 filler after the same ageing time. Pavan et al. [23] also testified the IN617 filler as an appropriate filler to produce the joint of austenitic steel with IN617 alloy and manufactured the welds joint which qualified the AUSC boiler requirements in the stress rupture test. Zhang et al. [24] produced a similar joint of heat-resistant steel using the IN617 filler and concluded that the migrated grain boundaries (MGBs) formed in weld metal were the major source of cracks during tensile testing at high-temperature. The poor impact strength near the interface was also measured and attributed to macrosegregation formed at the interface as a result of welding. Autogenous Laser welding was also done to produce the dissimilar weldments of P92steel/IN617 alloy [25]. The mechanical test showed that the weld joint has sufficient integrity to sustain the load. However, macrosegregation still existed at the interface of weld and BMs. Naffakh et al. [26] assessed the mechanical performance of the dissimilar weld joint (DWJ) between 310SS and Inconel 657, varying the filler composition. From the results, it was inferred that the formation of the low melting Cu-rich phase in 310SS filler makes the weld metal highly susceptible to hot cracking while considerable embrittlement was observed for IN617 filler due to dendritic microstructure. The Inconel 82 filler was testified as the greatest choice for making the DWJ. Ding et al. [27] investigated the impact toughness of the IN617 HAZ as a function of ageing time for a DWJ of 9% Cr steel/IN617. A minor impact on the impact toughness of the weld zone was observed with ageing, whereas a continuous decrease in impact toughness was measured

for the IN617 HAZ with ageing time, attributed to the formation of lamellar carbides. In addition, some researchers have conducted a study on the creep behaviour and residual stress variation along the weldments. In DWJ of P92 steel/Inconel alloy, the failure during creep condition happened either from the region of ICHAZ of P92 referred to as Type IV cracking [28] or from the interface region of P92 and weld metal due to the formation of oxide notches [28]. Zhang et al. [9] reported the failure of the DWJ of 617 B and modified 9%Cr in creep exposer condition either from BM and ICHAZ of P92 or from the interface. The creep test results showed that failure from the ICHAZ was mainly caused by matrix softening and poor availability of the grain boundaries pinning particles while the failure at the interface was attributed to the formation and growth of oxide notch. Shin et al. [29] also evaluated the creep performance for DWJ of Inconel 740H produced using the fusion welding process with IN82/182 filler. The interfacial failure was observed mainly due to the high creep strength gradient across the interface while Type IV failure, i.e. failure from ICHAZ was diffusion controlled which led to the localized strain at the small grain boundaries and weakening of the grain boundaries. Wu et al. [30] reported that the evolution of Laves phase and coarsening of the $M_{23}C_6$ phases during creep exposure contributed to the softening of the matrix and facilitated the crack initiation that caused the failure of the DWJ of Inconel 625–9% Cr steel from the HAZ of steel. The residual stress measurement across the welded joint of P92/IN625 alloy using the deep hole drilling (DHD) and newton diffraction (ND) methods. The residual stresses in weld metal were measured in the range 0f 350–450 MPa for as-welded joints and get reduced significantly after the PWHT. Nowadays, DHD is the most popular technique for the measurement of residual stress as it provides the measurement along depth [31]. The effect of the groove geometry has also reported a significant impact on the magnitude and nature of the residual stresses in DWJ [31]. Lee et al. [32] performed the residual stress measurement in DWJ of P92/IN617 alloy for U type of groove geometry produced using the GTAW process with Thysen 617 filler. The distribution of residual stress was measured higher on side of P92 steel than alloy 617. The weld residual stresses were 298 MPa and 245 MPa in the longitudinal and transverse directions, respectively. Few studies have also bene published on residual stress variation along the DWJ of P92 steel and SS304H steel in which measurement was performed using the DHD [33].

As evident from the literature study, the DWJ of P92 steel and IN617 is highly applicable in AUSC power plants. However, it is difficult to make a joint of two materials due to the variation in CTE, chemical composition, and microstructure. Few studies have been reported on DWJ of P92 steel/IN617 alloy including the filler selection, creep performance, and residual stress variation. However detailed investigation is still not available in the public domain. Therefore, the development of joining technology and a detailed investigation of the DWJ is essential. The effect of the weld groove geometry and filler composition on the structural integrity and microstructure evolution has been investigated for the DWJ of P92/IN617 alloy. Additionally, the influence of groove geometry on residual stresses was investigated for both as-welded and post-weld heat-treated (PWHT) joints.

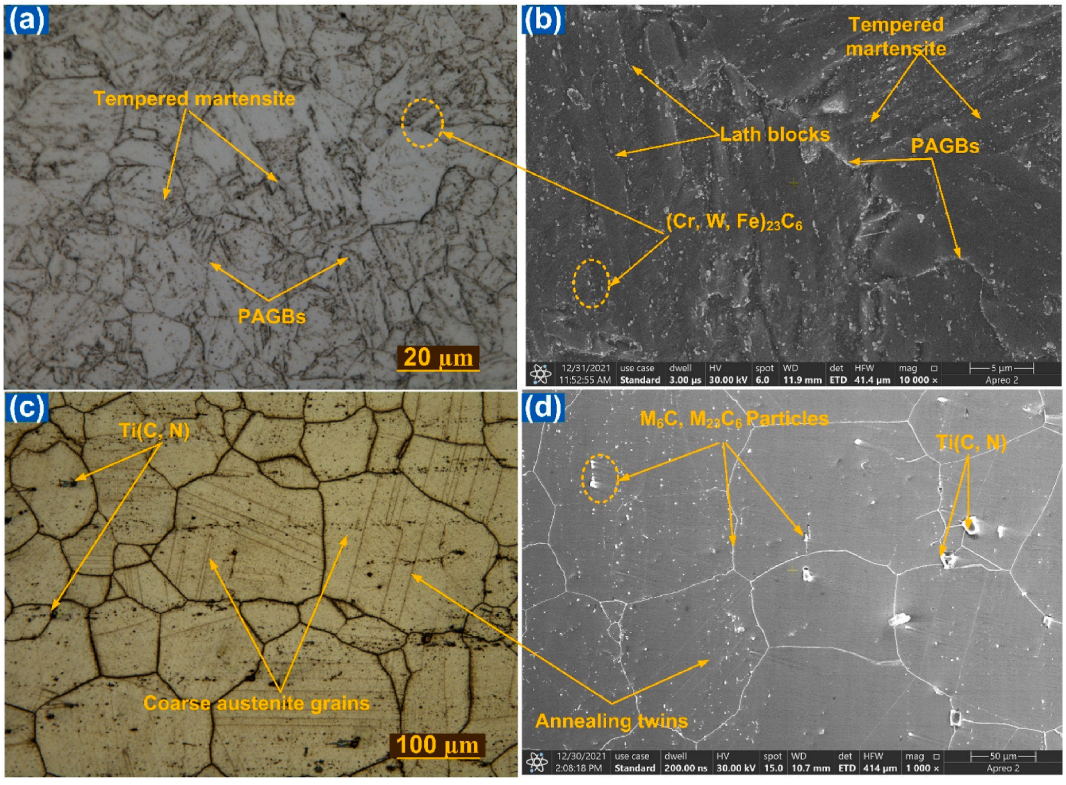

Fig. 1. Typical optical and SEM image of base materials (a, b) P92; (c, d) IN617 alloy.

1.1. Welding

Inconel 617 alloy and P92 steel plate of thickness 10 mm were machined for the experiment. P92 steel contains tempered martensitic microstructure (Fig. 1a). The optical image shows the distinct feature of lath blocks, and prior austenite grain boundaries (PAGBs). The distribution of the precipitates along with blocks and PAGBs are displayed in Fig. 1b. The SEM image shows the presence of coarse particles along the boundaries and lath blocks while fine precipitates are seen within the matrix. The EDS results of coarse particles ensured that precipitates are Cr, Fe, and W-rich carbides (Table 1). The fine precipitates were quantified by TEM analysis and confirmed as carbonitride of type MX and enriched with V and Nb [34]. A typical austenitic microstructure consisting of annealing twins and coarse austenite grains was seen from the optical image of IN617 alloy (Fig. 1c) [35]. The boundaries and matrix are accompanied by precipitates as illustrated in Fig. 1d. The EDS of block shape particles (marked in Fig. 1c and d) confirmed the existence of the Ti-rich carbides and nitrides phases **(Table 1).** The occurrence of the coarse Ti(C, N) phase in IN617 alloy has also been confirmed from the previously published work [36,37]. The distribution of fine particles in inter and intra-granular areas of the matrix is displayed in Fig. 1d. From the EDS result, it is inferred that the weight percentage of the Cr and Mo is high in grey particles while white coarse particles have a major weight percentage of Mo (Table 1). The grey particles might be of Cr and Mo-rich $M_{23}C_6$ and the white particles might be of Mo-rich M_6C. The previous study of Ren et al. [38] and Pavan et al. [23] also observed the phases of Cr-rich $(Cr, Co, Mo)_{23}C_6$, Mo-rich Mo_6C, $(Mo, Cr, Si)_3(Ni, Co)_3C_6$, or $(Ni, Co)_3Mo_3C$ and Ti-rich Ti(C, N) in IN617 BM. Ren et al. [39] reported that the precipitates of type $M_{23}C_6$ decorated along the grain boundaries provided the pinning effect to grain boundaries and increased the high-temperature creep strength of the IN617 alloy. A similar observation has also been made in previous study [40,41].

To prepare the butt weld joint of two dissimilar plates, two different groove configuration was used: one was a universal conventional V groove (VG); the second one was a narrow V groove (NVG) (Fig. 2a and b). The plate after groove cutting is displayed in Fig. 2(c and d). The weld joint of the plates was devised using the Gas Tungsten Arc Welding (GTAW) process with Inconel 82 (ERNiCr-3) filler of diameter 2.4 mm. Table 2 displays the composition of the base plate and filler metal. Before joining, plates were cleaned using the SiC paper of grit size 200 and then cleaned with acetone solution to remove the surface asperities. After the cleaning, preheating of the P92 steel plate was done at 250 °C to minimize the problem related to hydrogen-induced cracking (HIC). Welding was carried out in a flat position with four passes (one backing; one capping and two center passes) for both the VG and NVG joints. The thoriated tungsten electrode EWTH-2 (98% W + 2% ThO_2) of diameter 1.9 mm was used to prepare the DWJ. Pure argon of purity 99.99% was used for shielding and purging purposes with a flow rate of 15 L/min and 10 L/min, respectively. After each pass cleaning of the surface was performed using the wire brush. The welding current for the root pass was kept at 160 amp and 150 amp for VG and NVG joints, respectively. The arc voltage and travel speed were ~16.7 V and ~85 mm/min for the VG joint. In the NVG joint, arc voltage and travel speed were ~16.5 V and ~82 mm/min. For the rest of the passes welding current, arc voltage and travel speed were 150 amp, ~16.2 V and ~80–90 mm/min, respectively in the VG joint. In the NVG joint, for the rest of the passes welding current, arc voltage and travel speed were 145–150 amp, ~15.8–16.2 V and ~80–85 mm/min, respectively. The heat input is calculated by equation (1) [42];

$$Hinput = \eta VI/S \tag{1}$$

where; where η, V, I, and S are the heat source efficiency (η = 0.6 in GTAW [43]), arc voltage, welding current, and travel speed, respectively. The overall heat input was 4.29 kJ/mm and 4.18 kJ/mm for VG and NVG joints, respectively. Two of the joints were prepared for conventional VG configuration while the other two joints were made for NVG configuration. The top and rear portion of the welded plate for both the groove joints is depicted in Fig. 2(e and f). Heat-treatment of the welded joint was also performed at 760 °C for 2 h to investigate the effect of tempering on mechanical properties and residual stresses.

1.2. Metallography and mechanical characterization

The macrograph of both the VG and NVG joint is displayed in Fig. 3(a and b). The weld metal corresponding to each pass and HAZ of P92 steel is marked in Fig. 3a-b. The P92 HAZ size for the subsequent filling pass was 5.04 mm and 3.71 mm for VG and NVG joints, respectively.

The opening of the groove after the completion of the welding was 17.04 mm and 14.19 mm, for the VG and NVG joints, respectively. To examine the microstructure along the weldments, a transverse cross-section (Fig. 4) was cut using wire-cut EDM and followed by mounting, sanding (up to 2000 grit size SiC paper), cloth polishing, and electro-etching (9 V and 45 s) in oxalic acid (10%) and water solution. To examine the P92 HAZ microstructure, weldments were etched in the Vilella solution. The microstructure feature was examined using the optical microscope (Leica DMC4500) and, Philips X130 scanning electron microscope (SEM). The transverse

Table 1
EDS results for P92 and IN617 BM (wt.%).

Phase (P92)	C	V	Cr	Nb	Mo	W	Fe
$M_{23}C_6$	4.26	0.38	12.45	0.12	4.82	3.62	74.35
Phase (IN617)	C	Cr	Ti	Co	Mo	Fe	Ni
$M_{23}C_6$	4.85	45.85	0.35	6.25	14.52	2.85	25.33
Ti(C, N)	–	12.45	55.8	4.85	12.85	1.45	13.5
Mo_6C	4.25	22.45	0.25	8.52	29.52	3.52	31.49

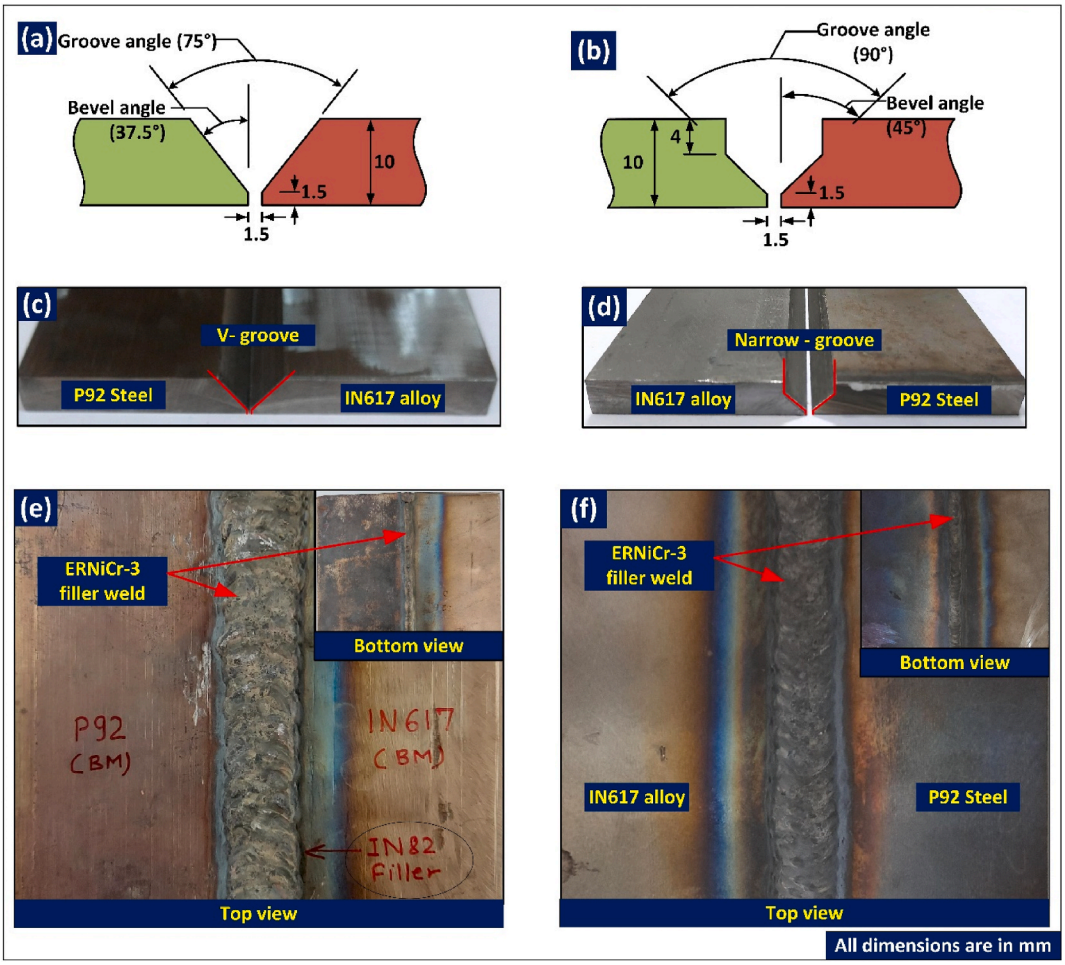

Fig. 2. Groove details: (a) conventional VG (b) NVG; (c, and d); (e and f) welded plate front and back view.

Table 2
Base metals and filler rod (ERNiCr-3) (wt.%) composition.

Elements	P92 steel BM	IN617 BM	ERNiCr-3 filler Nominal	ERNiCr-3 filler	ERNiCr-3 filler welds
C	0.093	0.058	0.1 max.	0.016	0.011
Si	0.210	0.001	0.5 max.	0.168	0.12
Mn	0.410	0.065	2.5–3.5	3.09	2.97
Cr	8.600	22.300	18–22	19.7	20.086
Mo	0.450	9.110	–	–	0.65
W	1.980	0.048	–	–	0.034
Ti	0.001	0.330	0.75	0.3	0.35
Ni	0.310	52.960	67 min.	73.9	68.29
Nb	0.052	0.016	2–3	2.45	2.24
V	0.180	0.110	–	–	0.031
Co	–	11.400	–	–	0.73
Al	0.001	1.460	–	–	0.19
Cu	–	0.016	0.5 max.	0.01	0.004
B	0.002	–	–	–	–
N	0.060	–	–	–	–
Fe	87.630	2.110	3 max.	0.132	4.27
S	0.004	0.005	0.015 max.	0.01	0.012
P	0.019	0.002	0.03 max.	0.01	0.003
Cr_{eq}	9.39	32.08	–	21.77	22.73
Ni_{eq}	5.11	54.73	–	75.92	70.10
Predicted microstructure	Martensitic	Austenitic		Austenitic	Austenitic

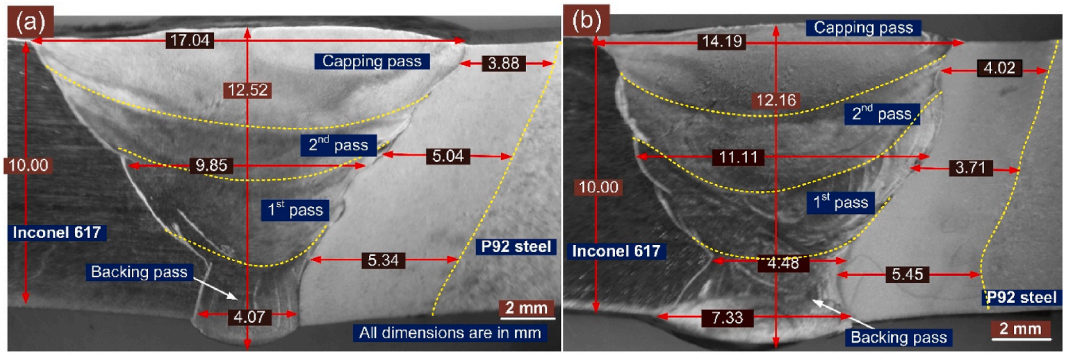

Fig. 3. Weld cross-section showing a sequence of welding pass, weld metal, HAZ, and BMs for (a) VG weld, (b) NVG weld.

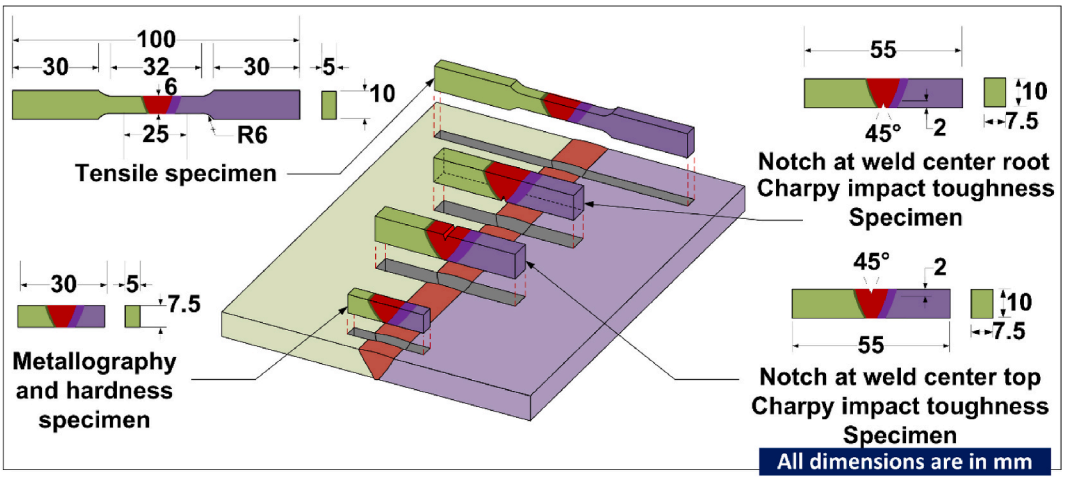

Fig. 4. Extraction of the testing specimen from the welded plate with their dimensions.

sub-size tensile specimens (length-100mm, gauge width-6 mm, gauge length-25 mm and thickness-5 mm) were cut from both VG and NVG joints according to ASTM E8/8 M [44] (Fig. 4). To maintain a constant strain rate during the tensile test, the extension rate was set at 1 mm/min. To estimate the impact toughness of the welds joint, an impact toughness specimen was prepared with a notch of 45° and a depth of 2 mm in the middle of the weld cross-section (Fig. 4) according to ASTM E23-02a [45]. The hardness measurement was done across the weldments at an interval of 0.5 mm and measured at three different locations (filling passes, capping pass, and backing pass) using the Vickers Microhardness Tester. The mechanical properties evaluation was done at room temperature and for each condition, three samples were tested. The residual stresses developed in the weld metal were calculated using the deep hole drilling (DHD) method [46].

2. Results and discussion

2.1. Solidification of weld metal

The cost of the ERNiCr-3 filler and the TEC in between P92 steel and IN617 alloy justified their selection as a filler metal. For BMs, filler metal, and solidified weld metal, the Cr_{eq} and Ni_{eq} were estimated and depicted in Table 2. The Cr_{eq} and Ni_{eq} value and their corresponding expected microstructure for BMs are given in the Schaeffler diagram (Fig. 5). The solidified weld metal showed the Cr_{eq} and Ni_{eq} of 22.73 and 70.10 along with a weight percentage of Ni of about 68.29% that confirming the austenitic mode of the solidification and fully austenitic microstructure for the weld metal. The weld metal has a weight percentage of Nb of about 2.24% which increases the degree of constitutional undercooling and results in a change in solidification mode (cellular to dendritic) [47,48].

According to Figs. 6 and 7, the Ni-based filler solidifies in an austenitic mode with three unique grain boundaries: the solidification sub-grain boundary (SSGB), the solidification grain boundary (SGB), and the migrating grain boundary (MGB). The sub-grains in the form of cells and dendrites represent the finest structure and are separated by the SSGB. The observed compositions are different at SSGBs than the bulk weld metal that is attributed to solute redistribution during solidification. The boundaries formed by the intersection of cells/packets of sub-grains are termed the SGBs and exhibits both compositional and crystallographic component. The

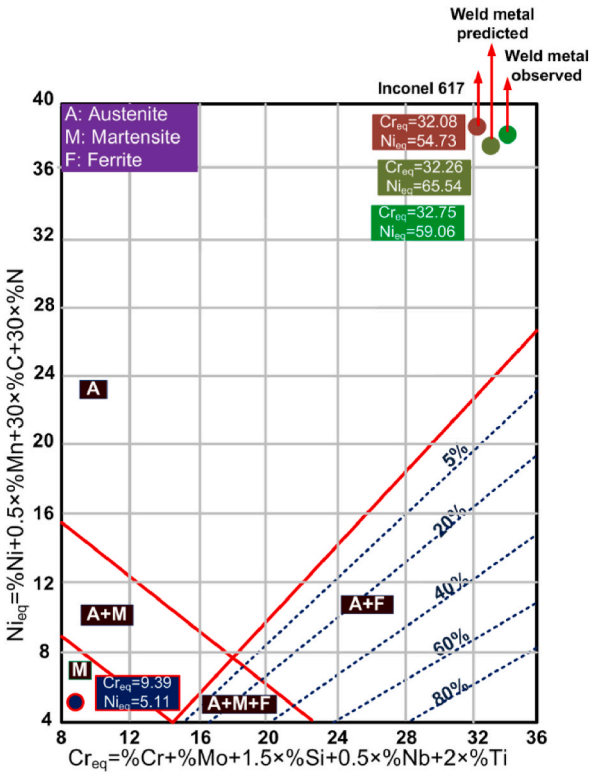

Fig. 5. Schaeffler diagram showing Cr_{eq} and Ni_{eq} value for BMs and ERNiCr-3 filler welds.

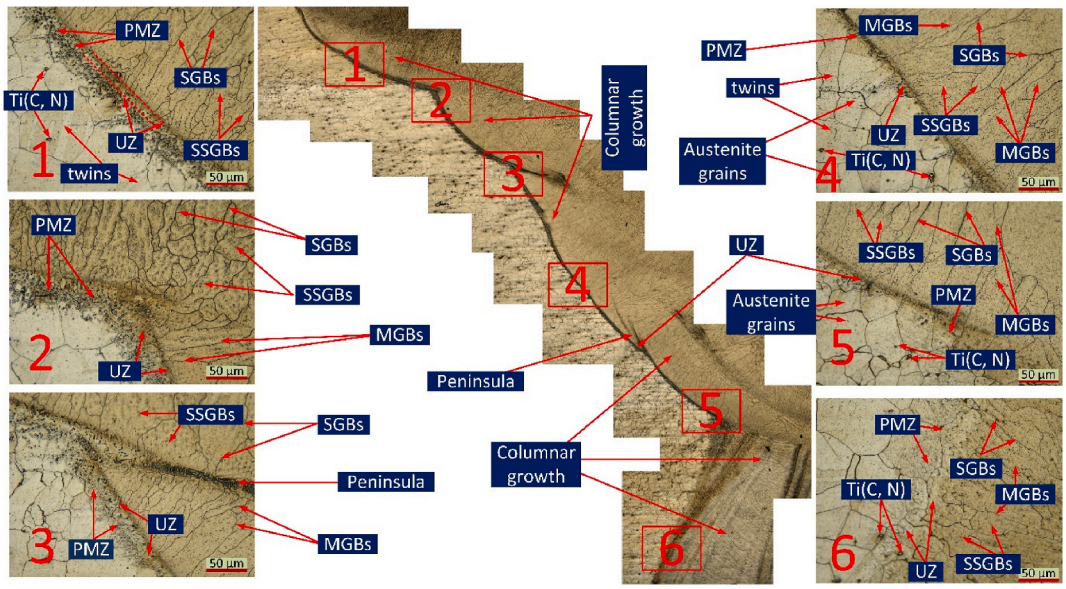

Fig. 6. ERNiCr-3 filler weld and IN617 alloy interface.

compositional components associated with SGBs are attributed to solute redistribution during solidification [49]. The subgrains of different orientations and growth directions create the high angular misorientation for SGBs due to it is also termed as 'high-angle' grain boundaries. The segregation of the impurity elements along the SGBs leads to the formation of the low-melting liquid film at end of the solidification and promotes the solidification cracking. Occasionally to lower the energy of the SGBs, the crystallographic component moves away from the compositional component and results in the development of the new grain boundary with less energy

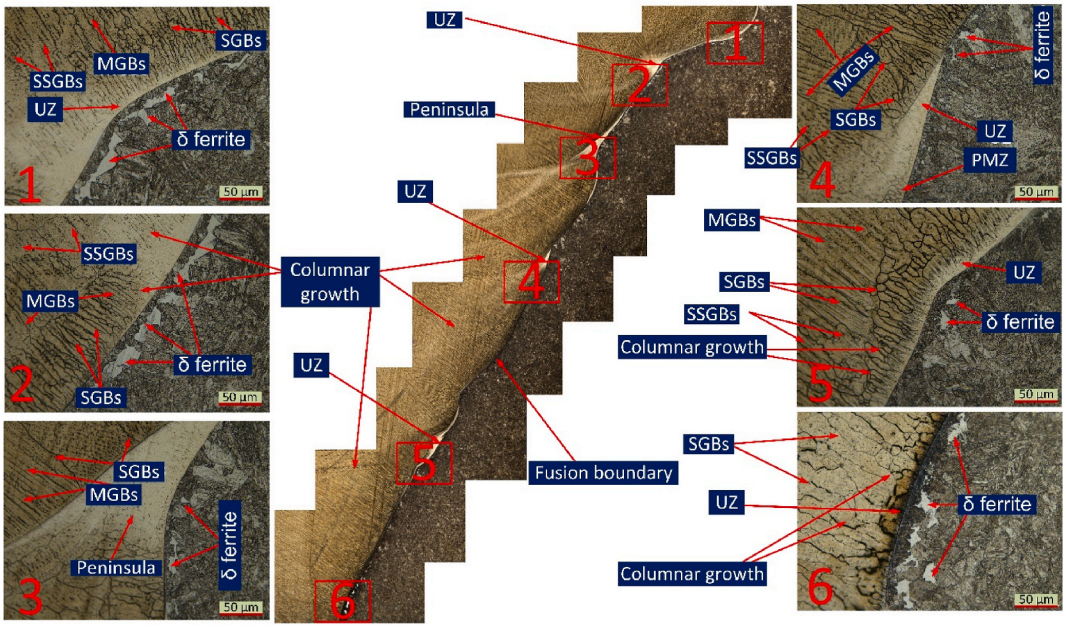

Fig. 7. ERNiCr-3 filler weld and P92 steel interface along the fusion boundary.

which is called MGB. The secondary phase formation across the SGBs and SSGBs stops the movement of the which results in the negligible formation of the MGBs. The ERNiCr-3 filler shows a higher number of MGBs and SGBs than the ErNiCrCoMo-1 filler because of the lower density of the effective pinning particles [12,40]. The weld metal adjacent to fusion boundaries is labelled in Figs. 6 and 7. The weld metal corresponding to the backing and capping pass (point 1 and point 6 in Figs. 6 and 7) shows a low proportion of the MGBs as compared to filling passes 1 and 2 (point 3 and point 4 in Figs. 6 and 7). The weld metal corresponding to filling passes 1 and 2 experiences the multiple welding heat cycles during the capping and backing passes which results in migration of the grain boundaries to lower its energy. In ERNiCr-3 welds, the formation of a higher number of MGBs makes it highly susceptible to ductility-dip cracking (DDC) as compared to ErNiCrCoMo-1 filler [40]. The P92 HAZ corresponding to the backing and capping pass shows the higher density of the soft δ ferrite patches (point 1 and point 6 in Fig. 7) as compared to passes 1 and 2 (point 3 and point 4 in Fig. 7). The lower density

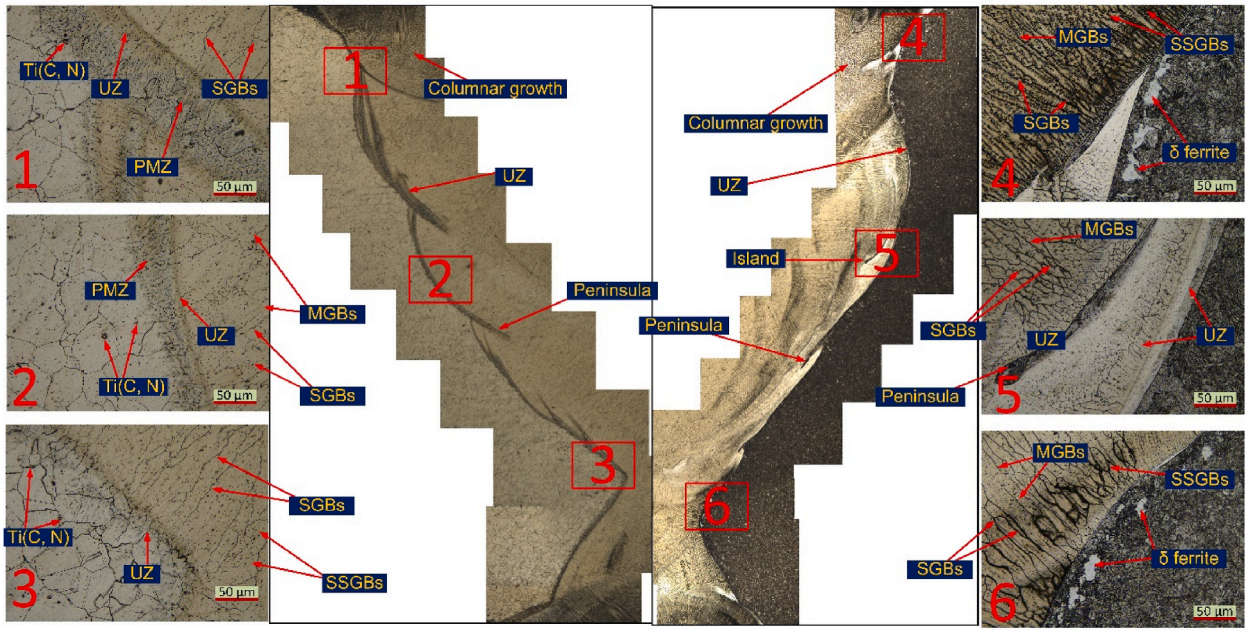

Fig. 8. Metallographic microstructures on both the side of the interface for NVG.

δ ferrite patches for pass 1 and 2 is attributed to the heating effect of the subsequent pass. The results showed good agreement with the report of Kumar et al. [50]. Near the interface of P92 steel, an unmixed zone (UZ) appeared vividly for the middle passes region. A non-uniformity in the thickness and shape of the UZ was measured along the interface. The swirls of BM are generated because of the fluid flow in molten metal and it causes detachment of BM which does not mix properly with bulk weld metal. Moreover, the formation of the UZ is promoted by the application of non-matching filler which is discussed later. Near the IN617 interface, a very narrow region of UZ and a partially melted zone (PMZ) are seen and the width of the zone remains almost uniform throughout the interface. The optical image near the interface is also captured for NVG design and presented in Fig. 8. A similar observation is made for NVG as observed for VG.

2.2. Characterization of interface and HAZ

The optical micrograph captured across the fusion boundaries for the VG welds joint (Fig. 9), ensured the inhomogeneity in microstructure across the weldments. Fig. 9 shows the formation of various zones across fusion boundaries for both IN617 and P92 BMs. Weld metal near interface and bulk weld metal have significant differences in microstructure in terms of grain boundaries, alloying elements segregation, and structure (Fig. 9). HAZ formed in P92 BM (as-welded specimen) is displayed in Fig. 9. As shown in Fig. 9, based on the distance from the fusion boundary, i.e. temperature practised during the welding process, the region can be divided into three sub-zones namely coarse-grained HAZ (CGHAZ), fine-grained HAZ (FGHAZ), and inter-critical HAZ (ICHAZ) as marked in Fig. 9. The CGHAZ adjacent to the fusion boundary experiences the maximum temperature among HAZ (>>A_{c3}) and permits the cessation of the carbide particles present in P92 BM ($M_{23}C_6$ and MX) and allowing the grains to grow as large size. The SEM image corresponding to mentioned CGHAZ (Fig. 10a) shows the coarse PAGs and lath blocks of different orientations with few undissolved precipitates within the lath blocks (top of Fig. 10a) which were confirmed as MX precipitates [34]. The FGHAZ next to CGHAZ shows a wide region and is formed at a temperature just above A_{c3} which enables carbide particles to dissolve partially in the matrix. The undissolved carbide particles limit the grain growth and on subsequent cooling, it converts into the untempered martensite with fine equiaxed PAGs (Fig. 9). The SEM image corresponding to FGHAZ is displayed in Fig. 10b which shows the typical lath blocks along with undissolved coarse precipitates at PAGBs and fine precipitate inside along within the lath blocks and along block boundaries. Finally, the most interesting region of the P92 HAZ, i.e. ICHAZ forms next to over-tempered BM (Fig. 9) and is heated between the

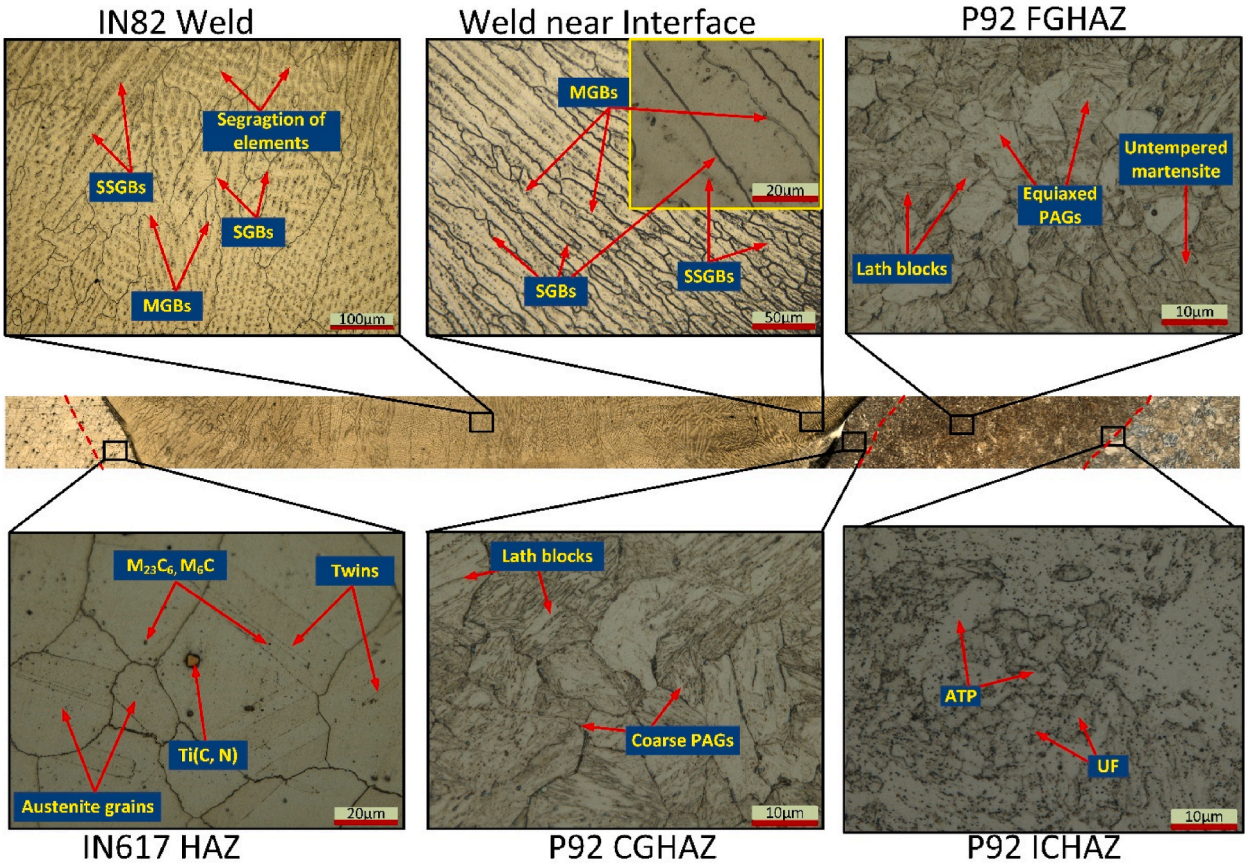

Fig. 9. Optical image of the dissimilar weldments in AW joint including weld metal at the center and near interface; HAZs of P92 steel and IN617 alloy.

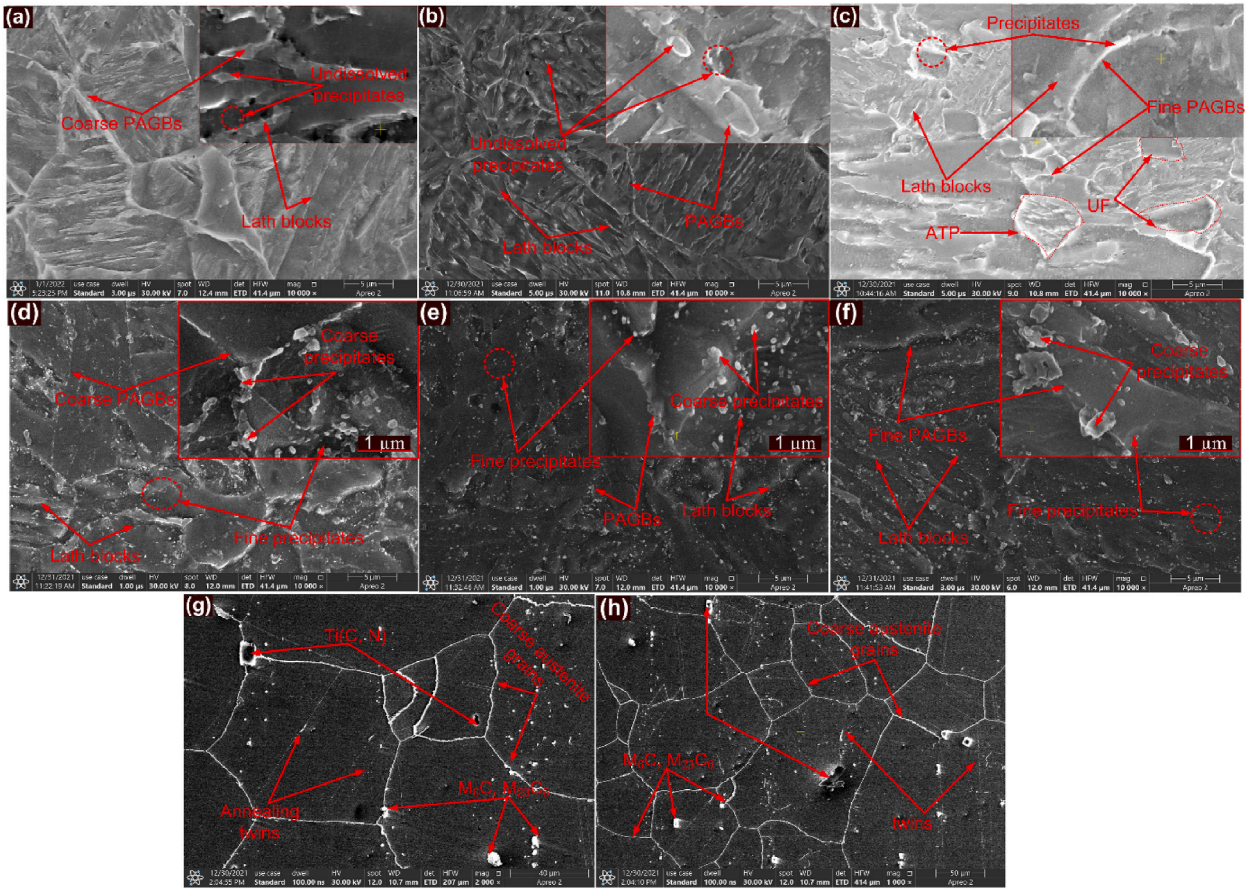

Fig. 10. AW joint: HAZs formed along P92 side (a, b, c); PWHT joint: HAZs formed along P92 side (d, e, f); IN617 HAZ: in the AW joint (g) and PWHT joint (h).

temperature A_{c1} and A_{c3}. The low-temperature results in the partial transformation from α to austenite are occurred during the cooling and are finally converted into untempered martensite, i.e. austenite transform product (ATP). The untransformed region of the matrix subjects to over-tempering and results in the formation of the untransformed ferrite (UF). The region of ATP and UF is marked in the SEM image as depicted in Fig. 10c. The precipitates in ICHAZ remain undissolved and result in grain interior and boundaries being accompanied by coarse existing precipitates as well as fine precipitates. A similar observation has been reported in previous study also for the HAZ of P92 steel [51]. The IN617 HAZ exhibits the austenitic microstructure having twins and precipitates along the austenite boundaries and grain interior (Fig. 9). The optical image of the IN617 HAZ (Fig. 9) and IN617 BM (Fig. 1a) shows a higher level of similarity, mainly due to the microstructure stability of the austenitic microstructure at high temperature. The minimum and maximum grain sizes were 35 µm and 92 µm, respectively and the average size was 56 ± 15 µm. The SEM image of the IN617 HAZ is depicted in Fig. 10g. The precipitates in IN617 BM are M_6C (small white particles), $M_{23}C_6$ (grey particles along boundaries), and Ti(C, N) (block-shaped) [52]. The welding heat results in the partial dissolution of the precipitates as stated by Hosseini et al. [53]. The dissolution of the Ti(C, N) was also reported by Gariboldi et al. [53] in the temperature range of 750–900 °C. However, Fig. 10g shows the bulky shape of the Ti(C, N) phase in the HAZ of IN617. The results shows the well agreement with previous observation [54]. The precipitates present in IN617 BM contribute to the strengthening and their dissolution may degrade the mechanical properties of the IN617 HAZ. The precipitates positioned along the boundaries were confirmed as lamellar carbides of Cr and Mo which have been reported an adverse effect on impact toughness as it acts as crack nucleation sites during impact tests at room temperature [27].

The main aim of the PWHT in the present work was to impart ductility to the untempered martensitic matrix in P92 HAZ and their effect is presented in Figs. 10 and 11. The elements dissolved in the matrix during the welding process come out in form of carbide and carbonitride during the tempering process in each region of P92 HAZ (Fig. 11a–c). The microstructure of CGHAZ and FGHAZ looks similar except for the grain size as it remains unaffected during the tempering process. The SEM image of CGHAZ and FGHAZ is depicted in Fig. 10d-e. The precipitate density at the triple point seems higher than the matrix region (Fig. 10d: top portion). The coarse precipitates, which are proven to be carbides of type $M_{23}C_6$, are primarily visible at the boundaries [34]. The coarsening of the precipitates is seen in the ICHAZ region (Fig. 10f) which occurs due to the combined effect of overheating during the welding cycle and over-tempering during PWHT. The region of IN617 HAZ exhibits the austenite grain, twins, and Ti(C, N), M_6C, and $M_{23}C_6$ precipitates as marked in optical (Fig. 11d) and SEM images (Fig. 10h).

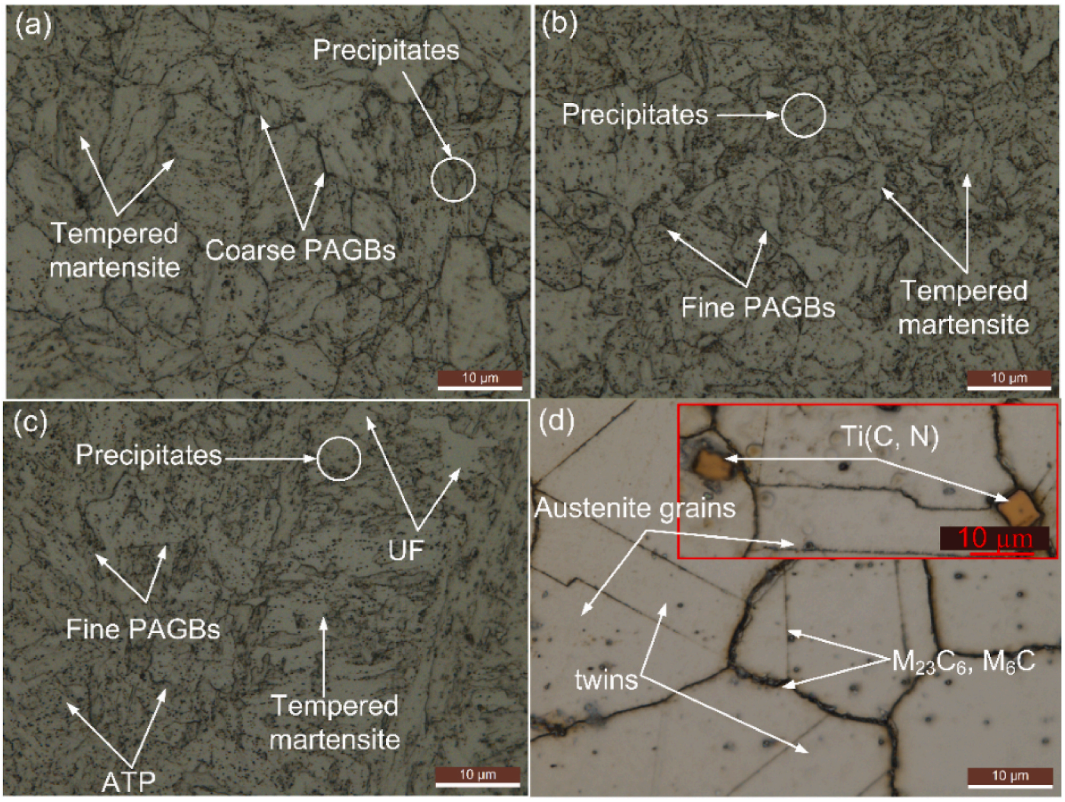

Fig. 11. PWHT joint: **(a)** P92 CGHAZ, (b) P92 FGHAZ, (c) P92 ICHAZ, (d) IN617 HAZ.

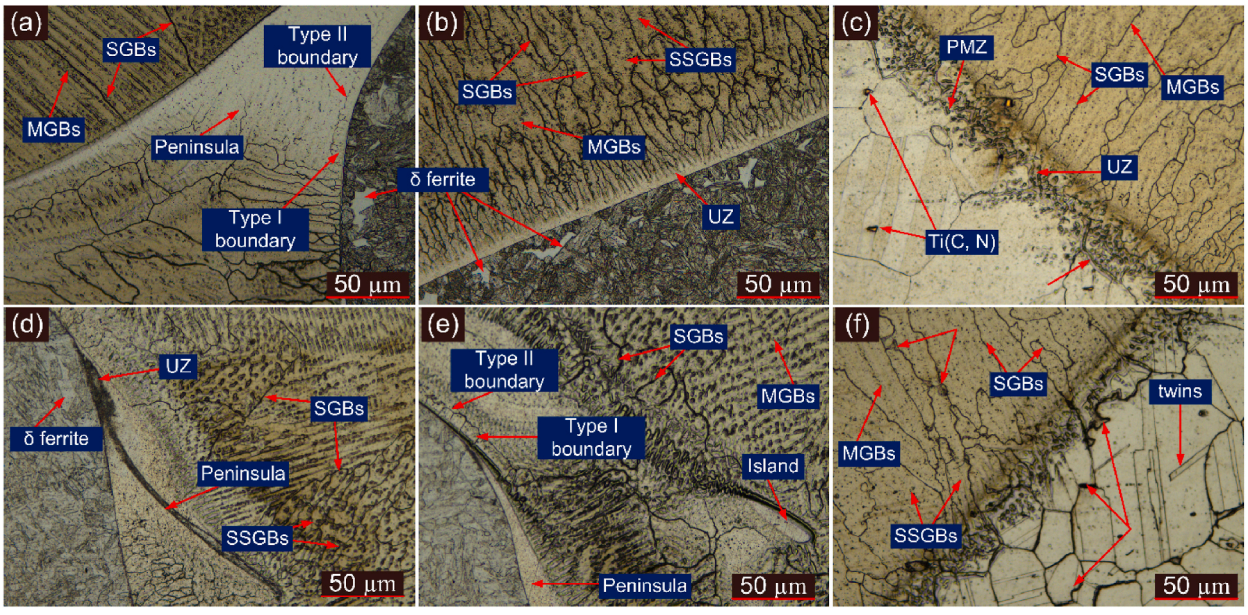

Fig. 12. AW: (a, b) Interface between the weld and P92 BM, (c) interface between the weld and IN617 BM; PWHT: (d, e) interface between the weld and P92 BM, (f) interface between the weld and IN617 BM.

2.3. Characterization of ERNiCr-3 filler welds and interface

The solute segregation occurs due to the inherent composition and melting point difference between BMs and filler metals and is reported as a serious problem in dissimilar welding of steel and Inconel alloy [55]. The features differ significantly from bulk weld metal in terms of composition and microstructure exists mainly at the fusion boundary and sometimes away from the fusion boundary. The features have identical nature to BM rather than the surrounding weld metal. The unmixed zone (UZ), the peninsula, and the island are the terms used to describe the macrosegregation features in the dissimilar welded joint that have already been reported [23,56,57]. The area near the fusion boundary consisting of such features is referred to as a filler-deficient zone. The formation of the macro-segregation has been elucidated by Kou and Yang [58] based on the liquid's temperature of base (T_{LB}) and weld metal (T_{LW}). The area of the filler deficient zone concerning the UZ is referred to as a peninsula and is otherwise referred to as an island [55]. UZ and peninsula are present at the P92 steel/ERNiCr-3 filler weld interface, as shown in Fig. 12a-b. The grain boundaries near to interface are also formed which grow parallel to the fusion line (Type II) and perpendicular to the fusion line (Type I) (Fig. 12a). The region of P92 HAZ has coarse PAGs within an untempered martensitic matrix and delta ferrite patches while ERNiCr-3 filler weld shows boundaries (SGBs and MGBs) and alloying elements segregation (Fig. 13a). The UZ along IN617 side (Fig. 12c) exists in the form of the laminar layers which are completely different in features of UZ formed along the P92 side. In addition, at the interface of IN617, there is the formation of the partially melted zone (PMZ) in which BM of IN617 gets heated below the liquidus temperature and above the solidus temperature which causes partial melting. At the interface of IN617, epitaxial growth occurs because of the similarity in microstructure (FCC) of both base and filler metal which facilitates the such type of growth. The Ti(C, N) precipitation in IN617 HAZ near the interface are also observed in both optical (Fig. 12c) and SEM image (Fig. 13b) which results in the thickening of the grain boundaries as marked in Fig. 12c. The macrosegregation feature has also been studied after the PWHT and displayed in optical (Fig. 12d–f) and SEM images (Fig. 13c–d). A filler deficient zone consisting of UZ, peninsula and island is seen on the P92 side (Fig. 12d–e). The boundaries (Type I and Type II) are also observed adjacent to the interface which is similar to the as-welded (AW) condition. After the PWHT, a thickening of the austenite grain boundaries in IN617 HAZ adjacent to interface becomes more pronounce and it might be due to the presence of both lamellar carbides and Ti(C, N) particles at the boundaries (Fig. 12f).

The alloying elements segregation and diffusion of elements across the interface have reported a severe effect on the creep properties. The SEM image of the interface and EDS results of each location including IN617 BM, IN617 HAZ, ERNiCrFe-3 filler weld, UZ, PMZ, and P92 HAZ is marked in Fig. 14a, b for the AW joint. Fig. 14a depicts the Cr, Fe, Ni, and Nb concentration across the P92 interface while the concentration of Cr, Fe, Ni, Nb, and Mo across the interface of IN617 is presented in Fig. 14b. As one moves from the P92 BM to the ERNiCr-3 filler weld, Fig. 14a shows a sharp increase in the concentration of Ni and Cr and a sharp decrease in the concentration of Fe, ensuring the diffusion of Ni and Cr from the ERNiCr-3 filler weld to P92 and the diffusion of Fe from P92 to the

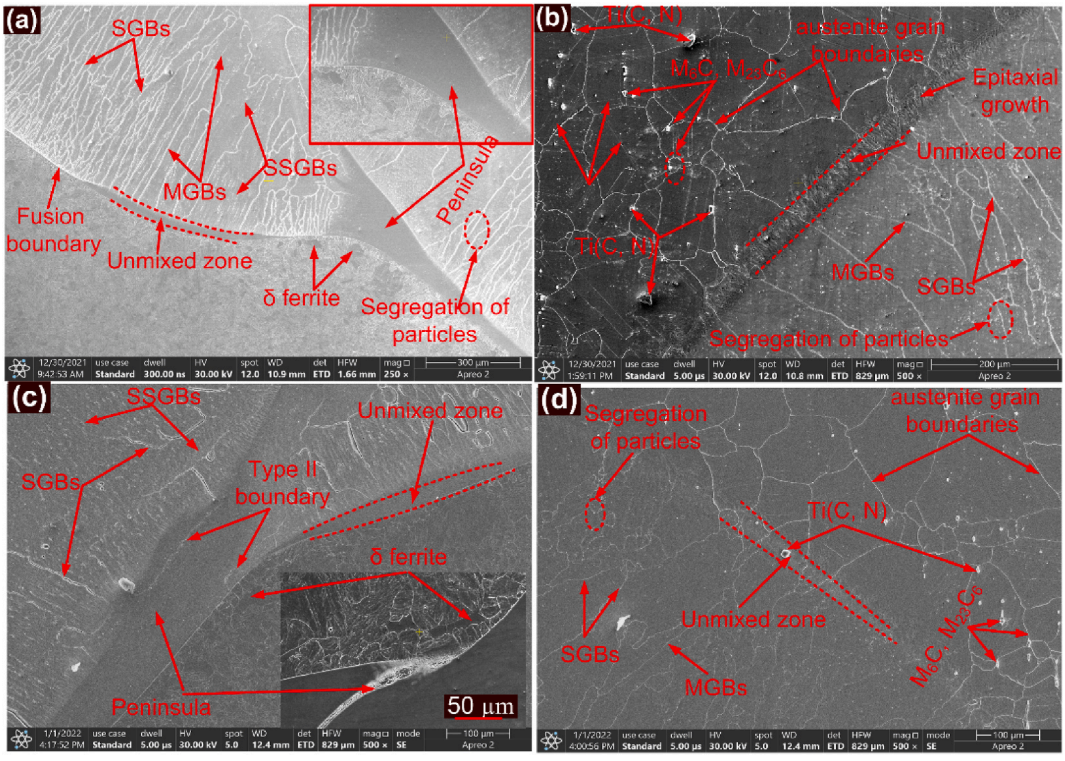

Fig. 13. Interface of weld and P92 BM (a:AW, c: PWHT); interface of IN617 ally and weld (c:AW, d: PWHT).

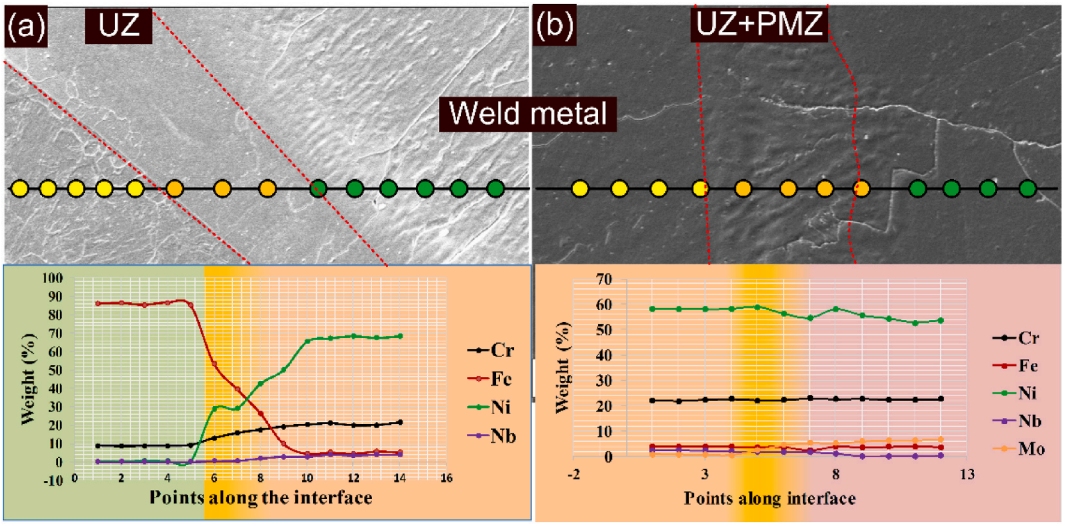

Fig. 14. AW: EDS line map on (a) P92 side, and (b) IN617 side.

ERNiCr-3 filler weld.

The concentration of Fe, Ni, Cr, and Nb in UZ was measured in-between P92 BM and ERNiCr-3 filler weld and delineated clearly in the weld interface band (Fig. 14a). The Cr diffusion from the weld to P92 steel may lead to the formation of Cr-rich carbide precipitates. The carbide formation in Cr–Mo steel HAZ in the dissimilar weld of T91/347H has also been confirmed from previously reported work

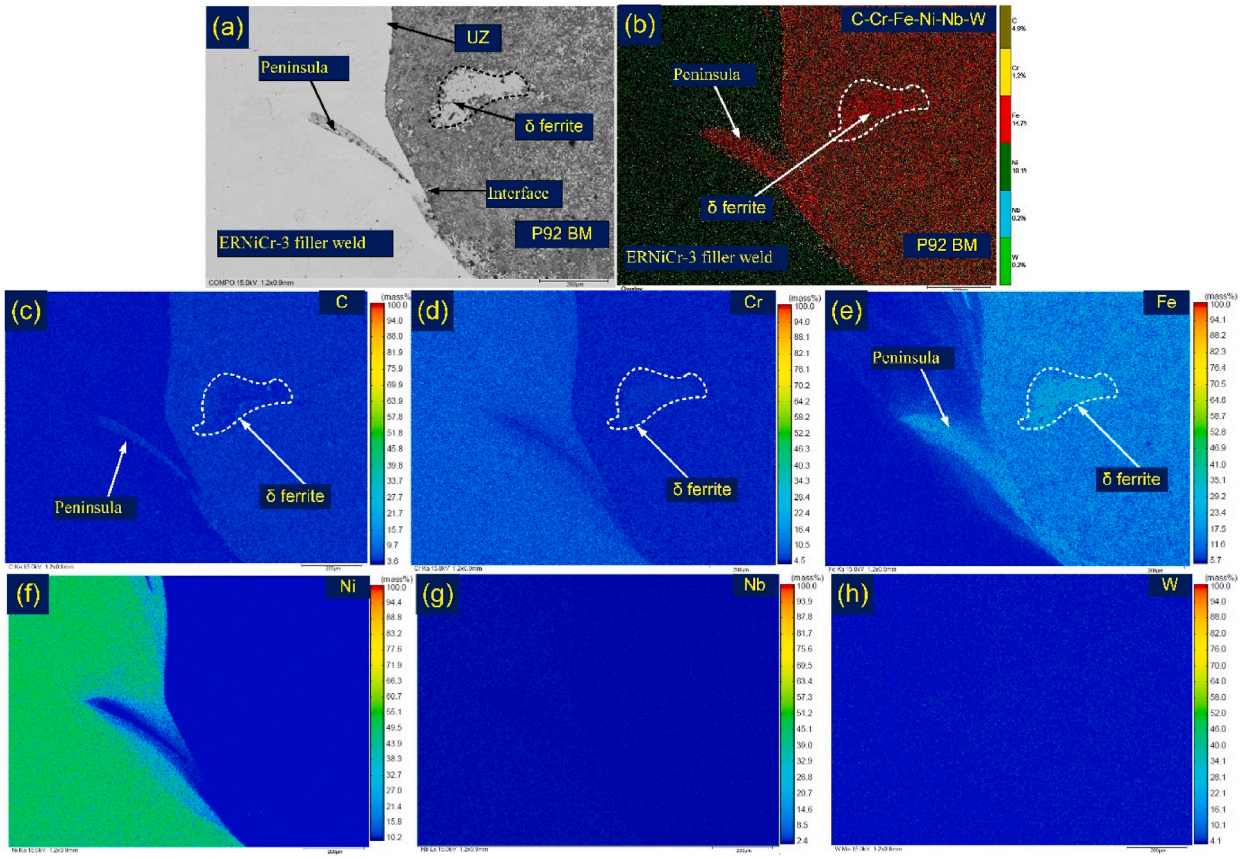

Fig. 15. AW: EPMA analysis of the unmixed zone at interface of P92 BM (a) morphology, EPMA map: (b) combine elements, (c) C, (d) Cr, (e) Fe, (f) Ni, (g) Nb, (h) W.

[17,59]. The major precipitates formed in HAZ were M(Cr, Fe)$_{23}C_6$ and Cr_7C_3 and Ni–Cr–Fe phase [17]. The diffusion of the elements is also confirmed by the EPMA map as given in Fig. 15a, b. Based on EDS and EPMA results, the formation of the different zone can be confirmed which are different in composition. The peninsula near the interface of P92 steel shows a higher concentration of C and Fe as given in Fig. 15c, e and certifies the similarity in composition with P92 BM. The δ ferrite near the interface and located in P92 CGHAZ have the major concentration of Fe and Cr and is depleted in C and Ni (Fig. 15c–f). The Cr-rich δ ferrite formation (Fig. 15d) is mainly supported by Cr depletion from the alloy matrix that ultimately affects the oxidation resistance [17]. Fig. 15g, h shows the distribution of the Nb and W at interface of P92 BM. Fig. 14b shows that the concentration curve of Fe, Ni, Mo, and Nb is smooth on the IN617 side interface which confirms a negligible diffusion of the elements across the interface. A negligible diffusion of the elements on the IN617 side interface is also proved by the EPMA map (Fig. 16a and b). The distribution of elements Fe, Ni, Cr, Co, Mo and Nb near IN617 interface is presented in Fig. 16c-h. That resulted mainly due to the similarity in microstructure and melting temperature of IN617 BM and ERNiCr-3 filler weld.

2.4. ERNiCr-3 filler weld

The micrograph of the ErNiCr-3 filler weld is taken corresponding to capping, filling, backing pass, and near the interface as delineated in Fig. 17a-f. The ERNiCr-3 filler weld microstructure is fully austenitic with 68.29% of nickel and has fine equiaxed dendrites. The 2.24 wt% of Nb in the weld causes the stabilization of the austenite at high temperatures. The Nb content in ErNiCr-3 filler also tends to enhance the degree of constitutional undercooling which results in a change in solidification mode from columnar/cellular to equiaxed dendritic [60]. The solidification mode in the weld fusion zone mainly depends on the involvement of the alloying elements and solidification conditions [61]. The dendritic microstructure scale is influenced by the cooling rate which is given by equation (2);

$$\text{Cooling rate } (^{o}C/s) = \text{Temperature gradient (G) } (^{o}C/m) \times \text{solidification rate (R) } (\mu m/s) \quad (2)$$

Hence, it is clear that the final grain structure is governed by G × R and higher G × R, i.e. fast cooling rate results in a finer grain structure. The other factor which plays a major role in solidification mode is alloying elements and in ERNiCr-3 filler, Nb plays an important role. Due to the tendency of Nb to increase the bulk solidification temperature range (increase in constitutional

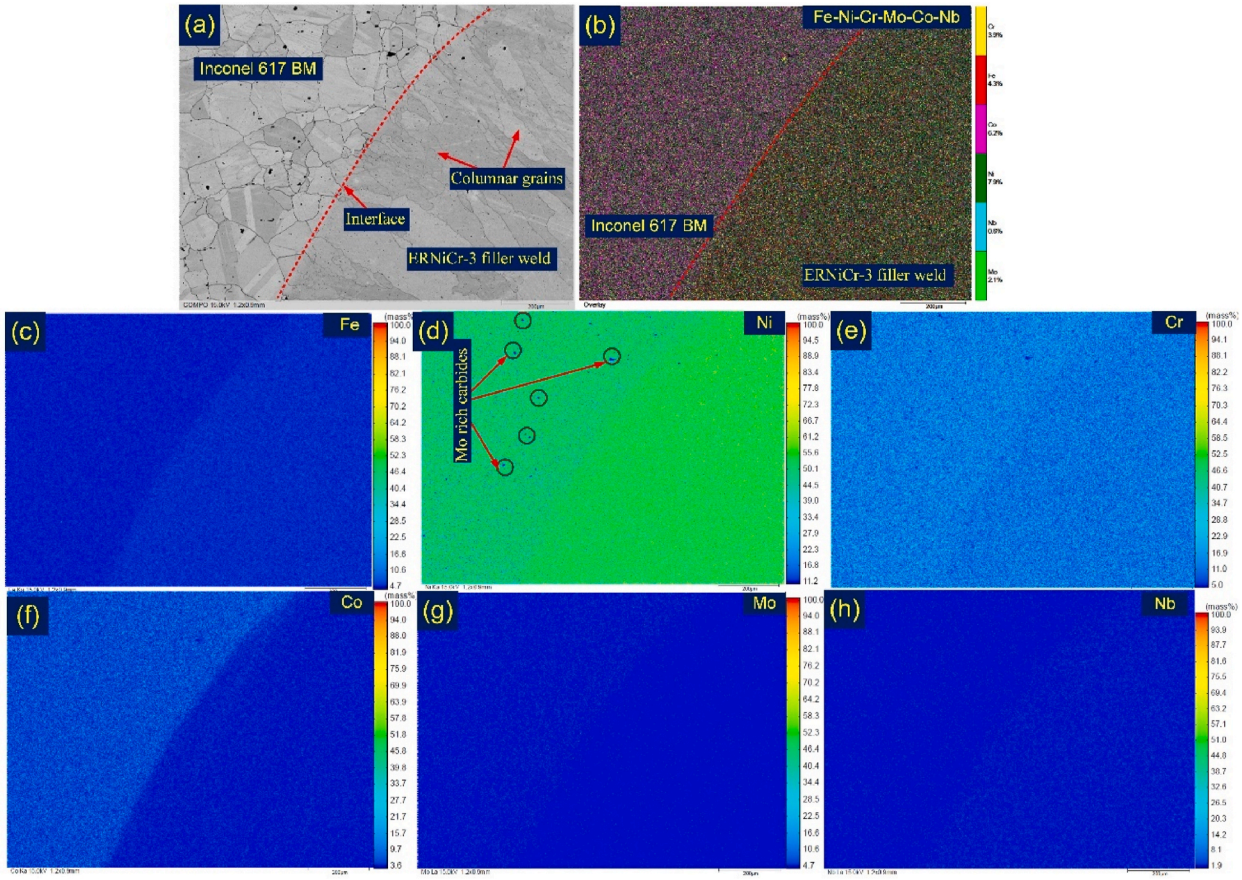

Fig. 16. EPMA analysis of the IN617 side interface (a) morphology, EPMA map: (b) combine elements, (c) Fe, (d) Ni, (e) Cr, (f) Co, (g) Mo, (h) Nb.

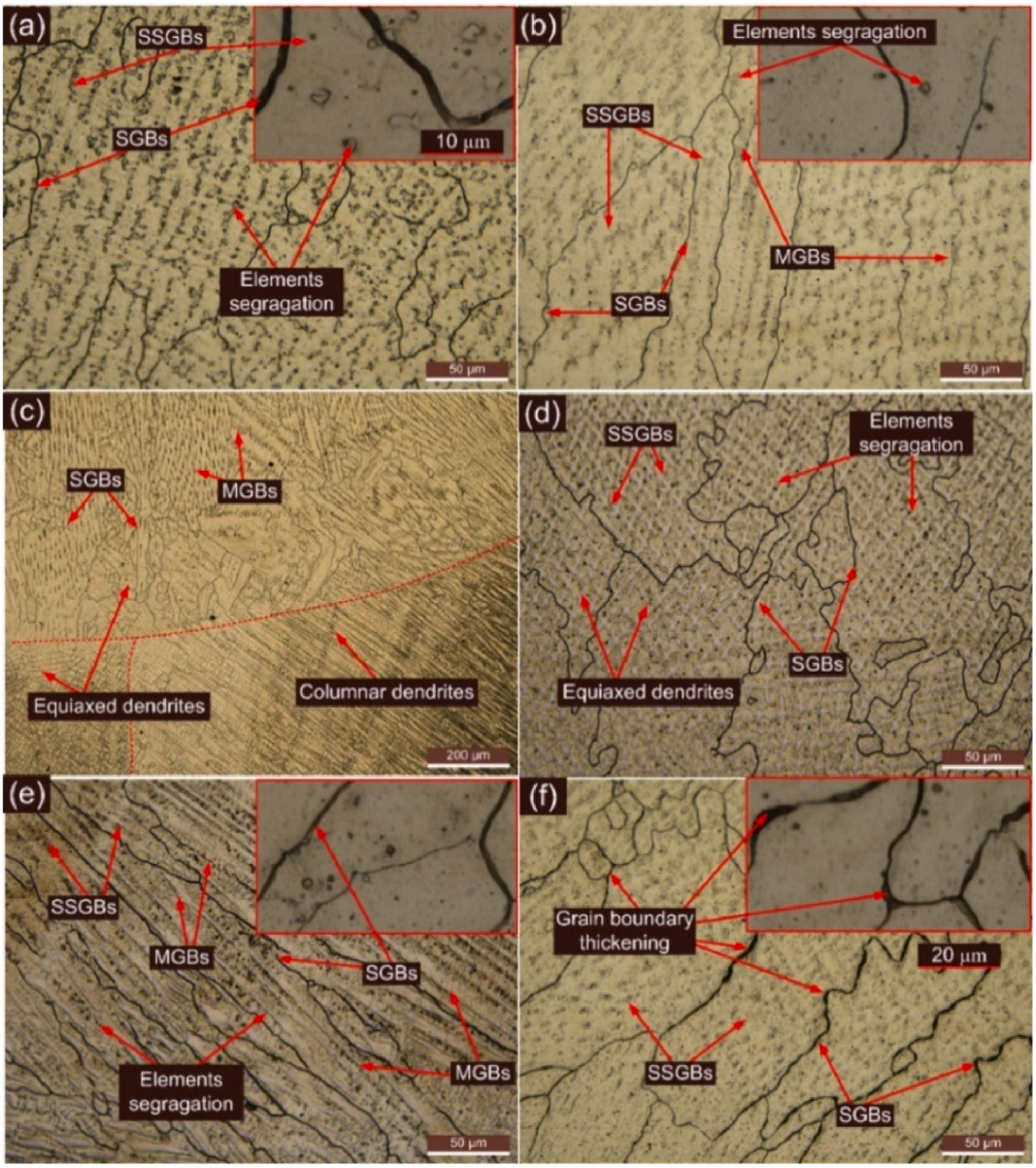

Fig. 17. Weld metal for AW joint: (a) capping pass, (b) filling pass, (c, d) backing pass, (e, f) weld metal near the fusion line.

undercooling), the substructure in ERNiCr-3 filler weld tends to change from cellular to columnar or from columnar to equiaxed [62] (Fig. 17a and b). The SGBs, SSGBs and MGBs are distinct in Fig. 17a-f. As compared to the ErNiCrCoMo-1 filler weld, the ERNiCr-3 filler weld displayed a high amount of the MGBs and this might be due to the less number of precipitates along the SGBs and SSGBs because these precipitates pin down the movement of the crystallographic component [40,55].

The ERNiCr-3 filler weld microstructure looks similar for both capping and filling passes except for the presence of MGBs in filling passes. The ERNiCr-3 filler weld corresponding to the filling pass (Fig. 17b) experiences multiple heating as compared to the capping pass (Fig. 17a) and it causes the migration of the crystallographic component from SGBs to lower its energy. That results in a higher number of MGBs in filling passes than capping and backing passes. The meeting point of the two passes shows similar microstructure characteristics like the interface of the ERNiCr-3 filler weld and BMs and it also imparts a great level of microstructural heterogeneity in microstructure (Fig. 17c). The boundaries between the two passes and microstructural heterogeneity across them are distinct in Fig. 17c. The ERNiCr-3 filler weld corresponding to the backing pass shows the finer dendrites as compared to filling and capping passes (Fig. 17d). A columnar grain structure of weld metal is seen near the interface (Fig. 17e and f). Also, the density of the grain boundaries near the interface is more than bulk weld metal. In some regions, the thickening of SGBs is observed which is attributed to the formation of Ti and some other low-melting precipitates [12].

The SEM image of ERNiCr-3 filler weld and their corresponding location is mentioned in Fig. 18 which represents the distribution of

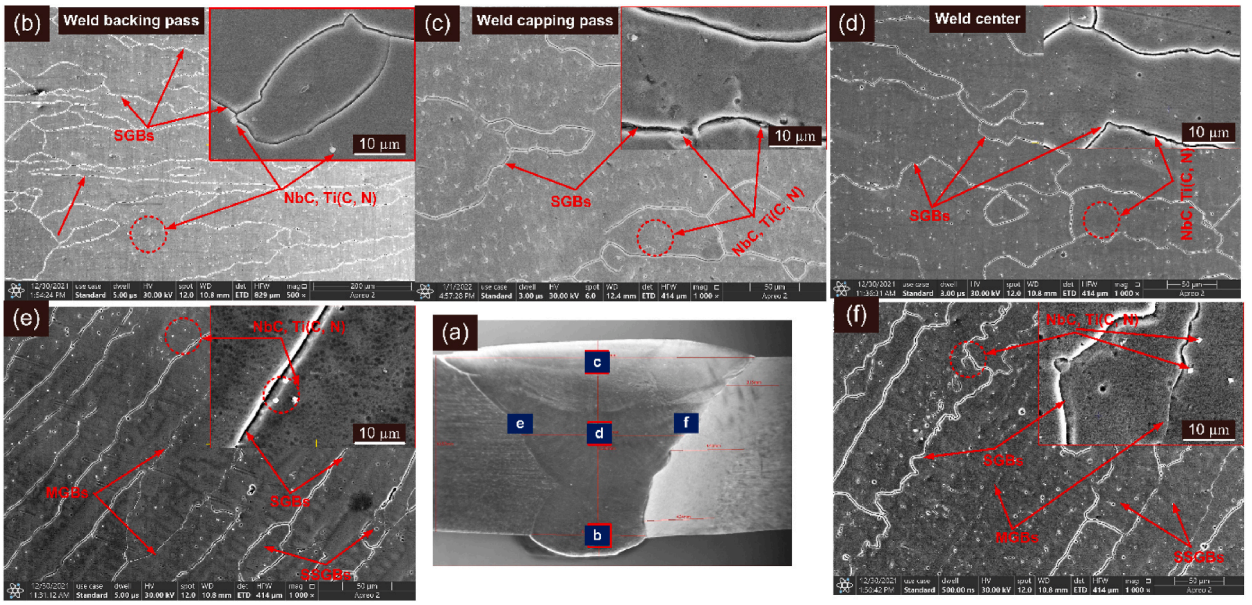

Fig. 18. Various regions of the weld metal in AW joint (a) macrograph showing location selected for SEM image, (b) backing pass, (c) capping pass, (d) weld center, (e, f) near the interface.

the precipitates at and around the boundaries. The boundaries in the backing pass are higher than in capping and filling passes as observed in the optical image (Fig. 18a–c). The boundaries and precipitates of shiny and dark are distinct in Fig. 18. The SGBs and inter-dendritic regions of the austenitic matrix exhibit a high density of the precipitates. The ErNiCr-3 filler weld near the interface

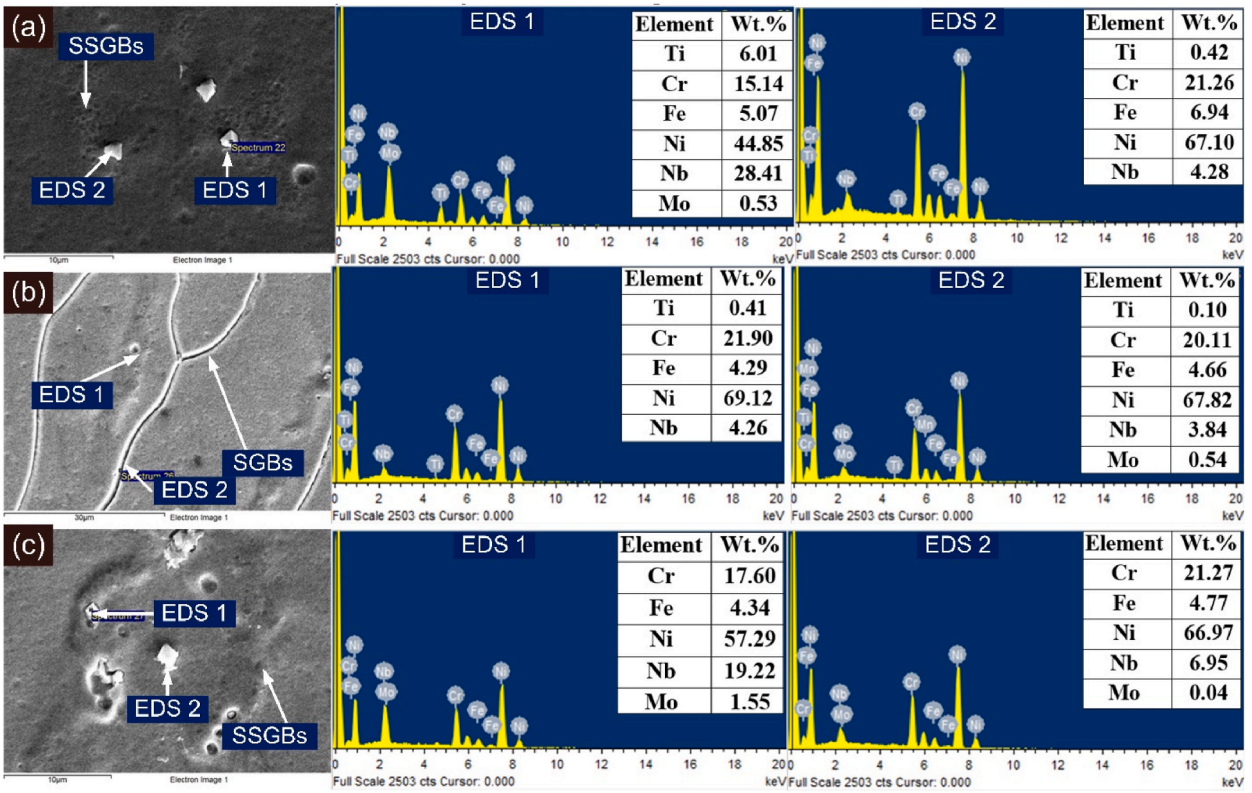

Fig. 19. Microstructure of ERNiCr-3 filler weld at different locations and corresponding EDS spectra of the precipitates: (a) backing pass, (b) weld center, (c) capping pass.

shows the columnar structure and a higher density of the precipitates is seen in inter-dendritic areas (Fig. 18e and f). The EDS results (Fig. 19a–c) reveal that the shiny precipitates are Nb-rich carbides (NbC) and the dark ones are Ti-rich TiC carbides. The EDS spectra of the precipitates and SGBs are observed for different locations of the weld metal and are presented in Fig. 19a-c. The evidence of the formation of the other phase like Laves is not found. The easy redistribution of the Nb at inter-dendritic areas is because of the poor equilibrium distribution coefficient, i.e. less than 1. The rejection of the Nb in inter-dendritic areas and diffusion of the C by interstitial mechanism results in NbC formation by reaction of Nb and C. Due to the formation of NbC at inter-dendritic areas, ERNiCr-3 filler weld shows a higher tendency of hot cracking [47] because it increases the solidification temperature range [63]. The Nb formation has also been found a negative impact on the ductility of the welded joint [60,64]. However, the formation of NbC increases the creep strength of the welded joint at high-temperature application [63] as it is known as the hardest intermetallic phase and processes the higher dissolution temperature. The EPMA results of the ERNiCr-3 filler weld are presented in Fig. 20a. The image utilized for the EPMA test is also mentioned in Fig. 20b which shows the distribution of the precipitates at SGBs and around them. From EPMA results (Fig. 20c–g) also it is inferred that the major precipitates in ERNiCr-3 filler weld are TiC and NbC. The distribution of the TiC particles is random while NbC is mainly seen along inter-dendritic spaces, i.e. SSGBs.

Fig. 21 represents the micrograph of the ERNiCr-3 filler weld after PWHT. The austenitic microstructure of the ERNiCr-3 filler weld does not show any major response to PWHT. However, the distribution of the NbC and TiC precipitates looks uniform as compared to the AW joint. The microstructure corresponding to the capping and filling pass (Fig. 21a–d) is equiaxed and coarse, for the backing pass microstructure is equiaxed and fine (Fig. 21e). Weld near to interface still shows the columnar dendrites and grain boundary thickening in some regions (Fig. 21f). The macrograph of the weld metal corresponding to each pass and near interface under SEM is presented in Fig. 22a. The weld near the interface still shows a higher number of grain boundaries than bulk weld metal (Fig. 22d and e). The precipitate distribution also looks uniform as compared to the weld metal of the AW joint (Fig. 22b–e). The boundaries and fine NbC and TiC precipitate at boundaries and inter-dendritic spaces are given in Fig. 22, corresponding to backing pass (Fig. 22b), capping pass (Fig. 22c) and weld center (Fig. 22d).

For the NVG joint, the optical image of weld metal corresponding to each weld pass is captured for both AW and PWHT (Fig. 23a–f). The microstructure is equiaxed austenitic and similar to the previous one. The boundaries corresponding to capping pass (Fig. 23a, d), center pass (Fig. 23b, e) and backing pass (Fig. 23c, f) are seen very clearly in optical image. However, the lower heat input in the NVG weld joint causes a higher cooling rate and results in the development of the fine and dense microstructure as depicted in Fig. 23a-f.

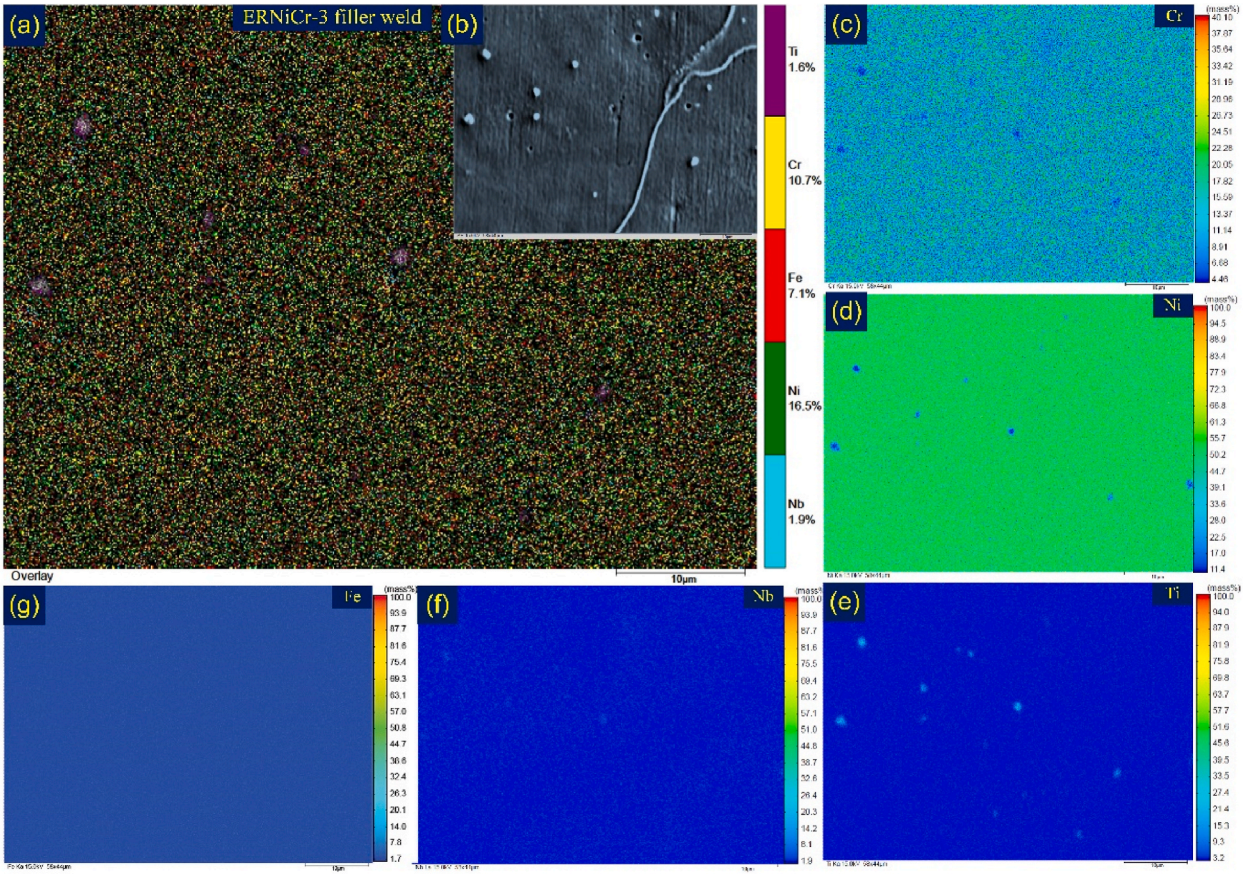

Fig. 20. EPMA analysis of ERNiCr-3 filler weld: (a) combine elements map, (b) morphology, (c) Cr, (d) Ni, (e) Ti, (f) Nb, (g) Fe.

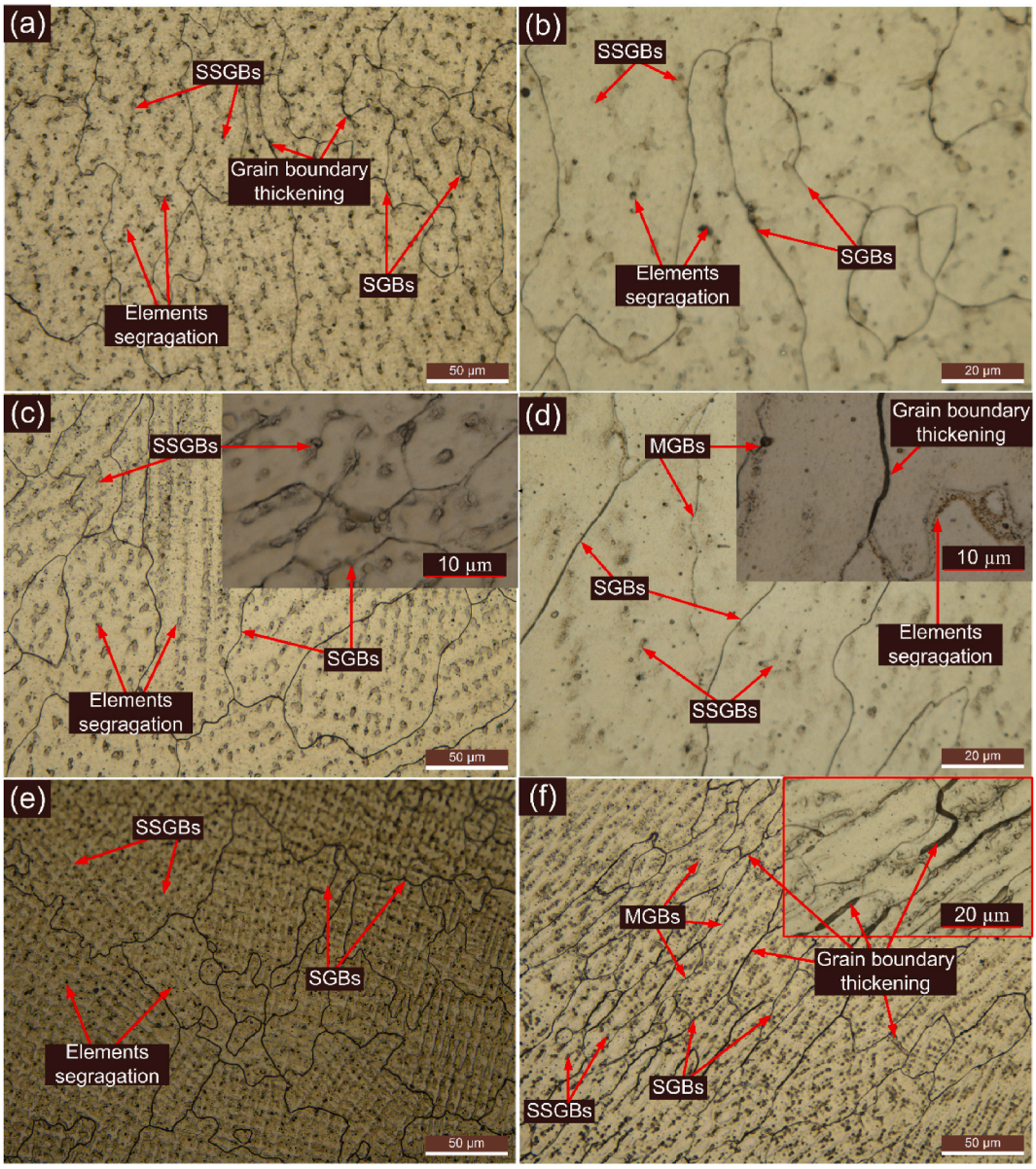

Fig. 21. Various regions of the weld metal in VG joint after PWHT (a, b) capping pass, (c, d) filling pass, (e) in the backing pass, (f) near the interface.

PWHT has observed a similar effect as seen in the VG weld joint. The boundaries are marked in each region (Fig. 23a–f)).

2.5. Mechanical properties assessment

2.5.1. Tensile properties

From the tensile test results (Table 3) of the dissimilar welded joints, it is inferred that fracture occurred from the ERNiCr-3 filler weld for all the trials of both the groove geometry. Tensile strength under AW circumstances revealed minimal variance in the test trials for VG and NVG welded joints. The fractured tensile sample and corresponding stress-strain curve are depicted in Fig. 24(a-c) for both AW as well as PWHT conditions. The tensile strength of 627 ± 2 MPa for VG and 636 ± 3 MPa for NVG welded joints has been observed. The test results along with the fracture region are depicted in Table 3. The tensile fractures appeared to be brittle for both the groove geometry as there was no significant plastic deformation, i.e. cup cone formation at the tip of the fracture surface. From the hardness plot, it was evident that ERNiCr-3 filler weld hardness is inferior to the other region of the weldments. It could be observed that there is a good agreement between the hardness results with the tensile strength of the weldments. As per the Han and Sun [65] report, it is a common exercise that the mechanical strength of the DWJ should be superior to the inferior BM. The tensile properties are

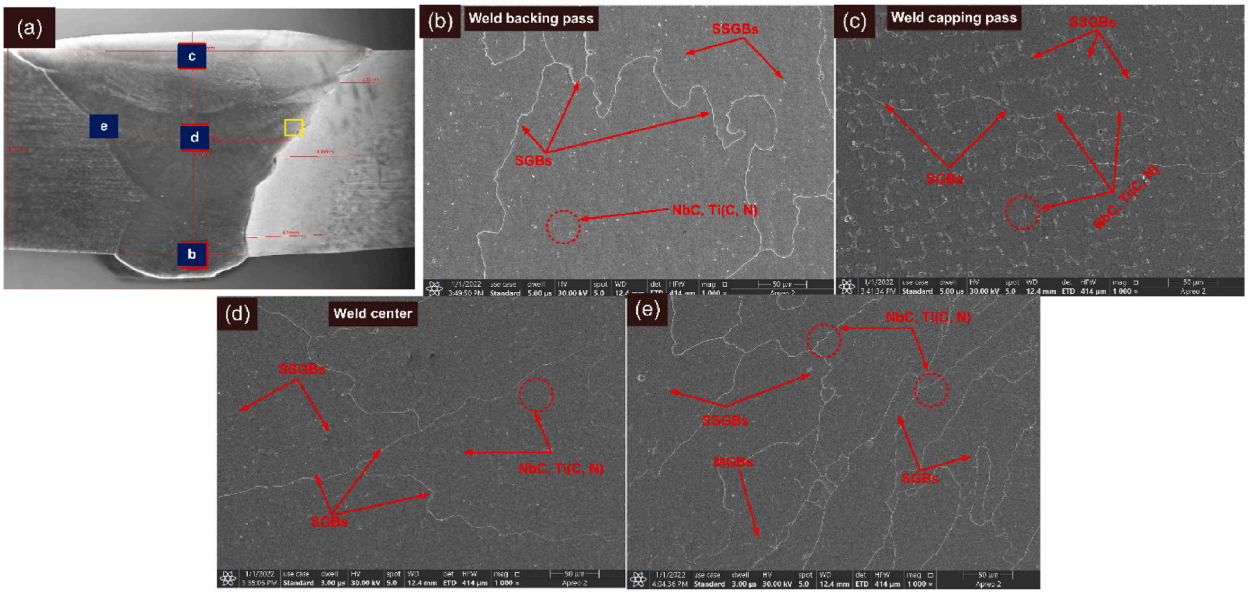

Fig. 22. Weld metal in VG after PWHT (a) Macrograph showing the location selected for SEM image, (b) weld backing pass, (c) weld capping pass, (d) weld center, (e) weld near the interface.

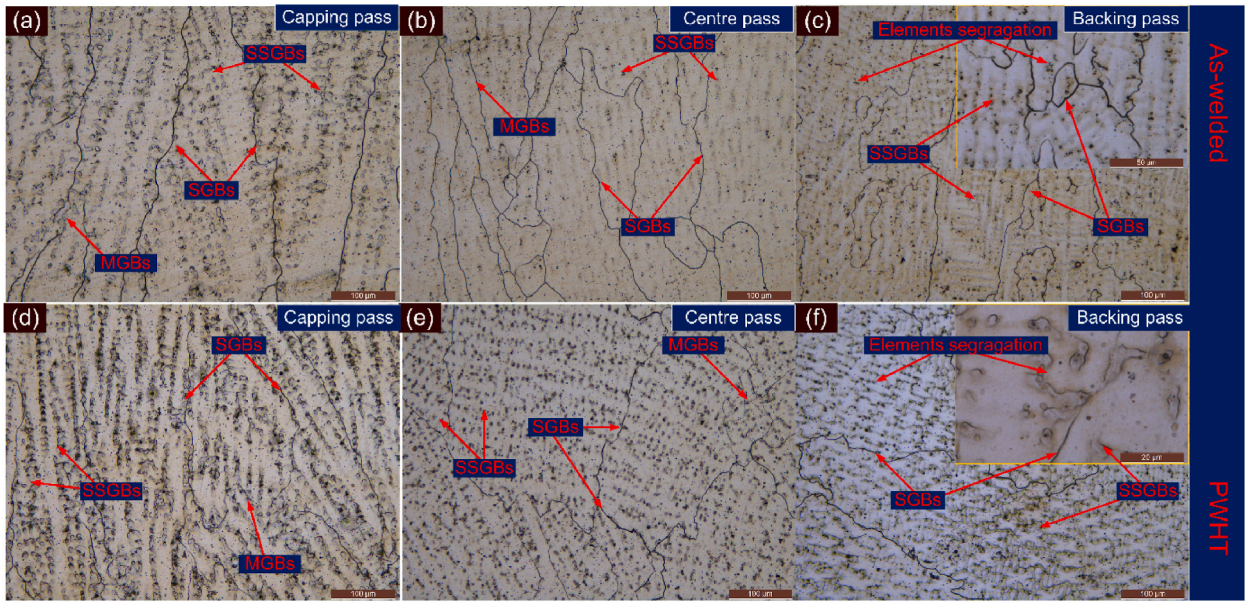

Fig. 23. Weld metal in the NVG before and after PWHT (a, d) capping pass, (b, e) center pass, (c, f) backing pass.

mainly influenced by the weld metal microstructure and its chemical composition. The austenitic microstructure was formed with a higher Ni content in ERNiCr-3 filler welds which offer a higher impact toughness however at the same time segregation of the Nb at the inter-dendritic areas reduces the tensile strength and also leads to the failure from the weld metal instead of weak BM. The VG welds joint was fractured from ERNiCr-3 weld metal, whereas the NVG welds joint failed either from P92/weld metal interface (trial 1) or from the weld metal (trial 2) in the AW state. The test specimens for NVG welds joint in PWHT state failed from the interface of P92/weld metal interface. For a similar weld joint of P92/IN617 alloy, the average tensile strength of 725 $\pm$ 5 MPa for IN617 filler weld [40] and 704 MPa for P92 filler weld [51] had been observed which was lower than the BMs, and also fracture occurred from the inferior P92 BM instead of weld metal. For both the groove geometry, the % elongation of the dissimilar weldments is less than P92 and IN617 BMs. The % elongation results confirmed that welded joints produced using the ERNiCr-3 filler are less ductile than the BMs, i.e. P92 and IN617 however, similar to the % elongation of the welded joint produced using ERNiCrCoMo-1 filler [40]. The PWHT resulted

Table 3
Tensile test results for VG and NVG welds joint.

Weld type		Conventional V groove weld	Narrow V groove weld	P92 BM	IN617 BM
Ultimate tensile strength (MPa)	AW	627 ± 2	636 ± 3	758 ± 6	777 ± 5
	PWHT	681 ± 12	643 ± 2		
Yield strength (MPa)	AW	335 ± 5	325 ± 5	520 ± 8	380 ± 8
	PWHT	362 ± 10	333 ± 4		
Elongation (%)	AW	26 ± 1	19 ± 2	33 ± 3	98 ± 4
	PWHT	31 ± 1	21 ± 2		
Reduction in the area (%)	AW	38 ± 1	40 ± 2	65.34	70.45
	PWHT	42 ± 1	41 ± 1		
Fracture location	AW	Weld metal	Weld metal or near P92 interface	–	–
	PWHT	Weld metal	Weld metal or P92 interface		
Joint efficiency (%)	AW	80.7	81.8	–	–
	PWHT	87.6	82.7		

in a drastic increase in the tensile strength of VG welded joints (681 ± 12 MPa) and a small increase in the tensile strength of NVG welded joints (643 ± 2 MPa). However, the % elongation remains almost unaffected for both the groove geometry. The fracture location is still noticed in the ERNiCr-3 filler weld.

The fractures specimen for the VG joint is characterized using the FESEM and displayed in Fig. 25. The tensile specimen was fractured from the weld for AW and PWHT joints where cellular or equiaxed structure along with Nb and Ti segregation was present. The fracture surface revealed the mixed mode of fracture and showed ductile dimples, cleavage area, and microvoids. However, the fractured specimen for the AW joint (Fig. 25a) showed a large area of dimples as compared to the PWHT joint (Fig. 25c). The area density of the microvoids was seen more for the PWHT tested specimen (Fig. 25c). The magnified view of the fractured surface showed the presence of the particles over the surface which are rich in Nb and Ti (Fig. 25b-d) and most likely to be carbides of Nb and Ti of type M(Nb, Ti)C. The EDS analysis of the fracture surface Fig. 25a-b shows the Cr, Mn, Fe, Ni, and Nb as major elements for both AW and PWHT. The Nb content in weld metal mainly increases the fragility of the welded joint. The Nb content reduces the tendency of ductile tear ridges formation [66] and ultimately encourages the inter-dendritic fracture as observed in the present investigation.

A high-temperature tensile test was conducted on the round specimen at 550 °C and 650 °C. Fig. 26 illustrates the outcomes obtained from testing weldments at high temperatures for both VG and NVG joints. To simplify the discussion, the welded joints tested at high-temperature 550 °C and 650 °C were denoted by VG-HT1 and VG-HT2 for VG welds joint and NVG-HT1 and NVG-HT2 for NVG welds joint, respectively. The test results showed the failure of the specimen from the P92 BM with the tensile strength of the 423 MPa and 258 MPa for VG-HT1 and VG-HT2, respectively and for NVG-HT1 and NVG-HT2, the tensile strength was 398 MPa and 276 MPa (Fig. 26a). Both VG-HT and NVG-HT exhibited a notable decrease in YS and UTS when compared to BMs, as revealed by the test outcomes. The observed decline may be attributed to the impact of softening and the heightened susceptibility to damage that occur at elevated temperatures. The stress-strain plot is mentioned in Fig. 26b. Based on the failure of the P92 BM specimen, it can be inferred that the Ni-based ERNiCr-3 weld has a superior yield and tensile strength compared to P92 BM. This is due to the exceptional deformation resistance of the weld at both room and high temperatures. The gauge area of the specimen consists of the weld metal, HAZ, and BM, each with its distinct microstructure and mechanical properties. As a result, the deformation of each zone during tensile loading will not be uniform and will be mainly controlled by precipitation strengthening and grain size. Between grain size and precipitation strengthening, the latter has been found to exert a more dominant effect in Ni-based filler. The % elongation was 16% for both VG-HT1 and NVG-HT1. For VG-HT2 and NVG-HT2, it was 18% and 14%, respectively (Fig. 26c). The % reduction in the crossectional area after the test is also mentioned in Fig. 26c.

The tensile fracture surface of the VG-HT and NVG-HT are further characterized and presented in Fig. 27a-d. Fig. 26a shows the macro-profiles of the fractured specimen and the variation in elongation across the gauge area. The fractured tip macrographs of the ruptured HT specimen are given in Fig. 27a-d. The average gauge diameter at the fracture frontier was also mentioned in Fig. 27. The macrograph (Fig. 26a) and top view of the fracture surface (Fig. 27a–d) show a cup-cone-shaped profile. The macro-profiles of both NVG-HT and VG-HT specimens reveal the presence of dimples and voids. The cup-cone formation with necking and the presence of higher-density dimples at the fracture surface is a characteristic of ductile fracture. The fracture surface of both NVG-HT and VG-HT exhibits a higher density of dimples and micro-voids as mentioned in Fig. 27a-d. However, dimples and voids are observed bigger in size for VG-HT2 and NVG-HT2 than VG-HT1 and NVG-HT1 (Fig. 27a–d).

2.5.2. Micro-hardness and impact properties

The hardness indentation was captured corresponding to each welding pass, as depicted in Fig. 28. The ERNiCr-3 weld metal hardness was 188 ± 5 HV and 202 ± 6 HV for the filling passes at two different positions as mentioned in Fig. 28a, b. The weld metal's average hardness was 207 ± 4 HV (Figs. 28c), and 189 ± 6 HV (Fig. 26d)for backing and capping pass, respectively. The in-homogeneity in the hardness value of the weld metal corresponding to each pass is attributed to the multi-pass nature of the welding which resulted in variation in the microstructure of weld metal in terms of boundaries, alloying elements segregation, etc. The hardness of the weld metal was observed lower than the P92 BM (240 ± 3 HV) and IN617 BM (214 ± 6 HV). However for IN617 filler, weld metal showed an average hardness of 211 ± 9 HV which is slightly higher than the ERNiCr-3 weld metal and also close to IN617 BM [40]. For BOHLER P92-IG filler, weld metal hardness was 458 ± 25 HV which was much higher than the Ni-based filler [40].

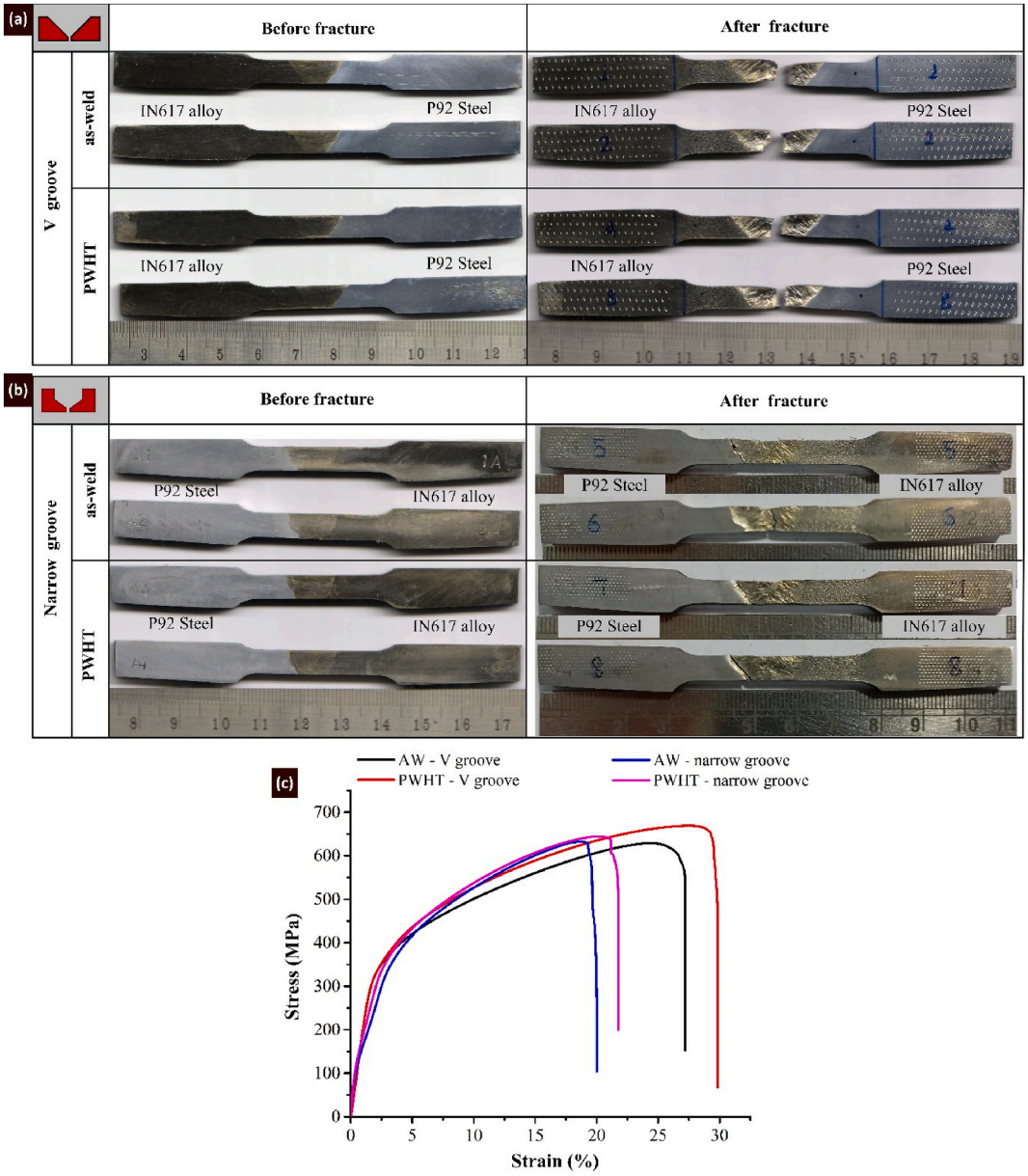

Fig. 24. Tensile specimen before and after fracture (a) VG welds joint, (b) NVG welds joint, (c) stress-strain curve.

The hardness indent for a different zone of the weldments is depicted in Fig. 29a, b. On both, sides of the interface, a dramatic change in hardness was observed. The hardness was 200 ± 3 HV and 209 ± 2 HV at the interface of P92 steel and IN617, respectively. On the P92 HAZ side, a significant variation in hardness was noticed which is attributed to microstructural change as discussed in Fig. 9. The region is very close to the interface, i.e. CGHAZ showed a hardness of 450 HV which was the highest among all the regions. The peak hardness in CGHAZ was due to the high content of C and N in the matrix which was obtained by precipitate dissolution at a high temperature (>>A_{c3}). The average hardness in FGHAZ was 414 ± 38 HV. The ICHAZ offers the minimum hardness among HAZs of P92 steel and it was 230 HV. The poor hardness, i.e. lower than the P92 BM was attributed to coarsening of the precipitates and grains and also the partial tempering of the martensite as discussed in the microstructural section. IN617 HAZ hardness (210 ± 3 HV) (Fig. 29a) was measured close to IN617 BM (214 ± 6 HV) and ensured the negligible change which is also witnessed from microstructural results.

After PWHT a mixed nature was seen and hardness variation along each pass is presented in Fig. 28a-d. The average hardness for the filling pass at two different locations was 205 ± 4 HV (Figs. 28a) and 198 ± 7 HV (Fig. 28b). It shows a significant increase, i.e. from 188 ± 5 HV to 205 ± 4 HV at location 1 (Fig. 28a) and a minute decrease at location 2, i.e. from 202 ± 6 HV to 197 ± 7 HV (Fig. 28b). The weld metal hardness for backing (Fig. 28d) and capping pass (Fig. 28c) was 209 ± 4 HV and 203 ± 3 HV, respectively.

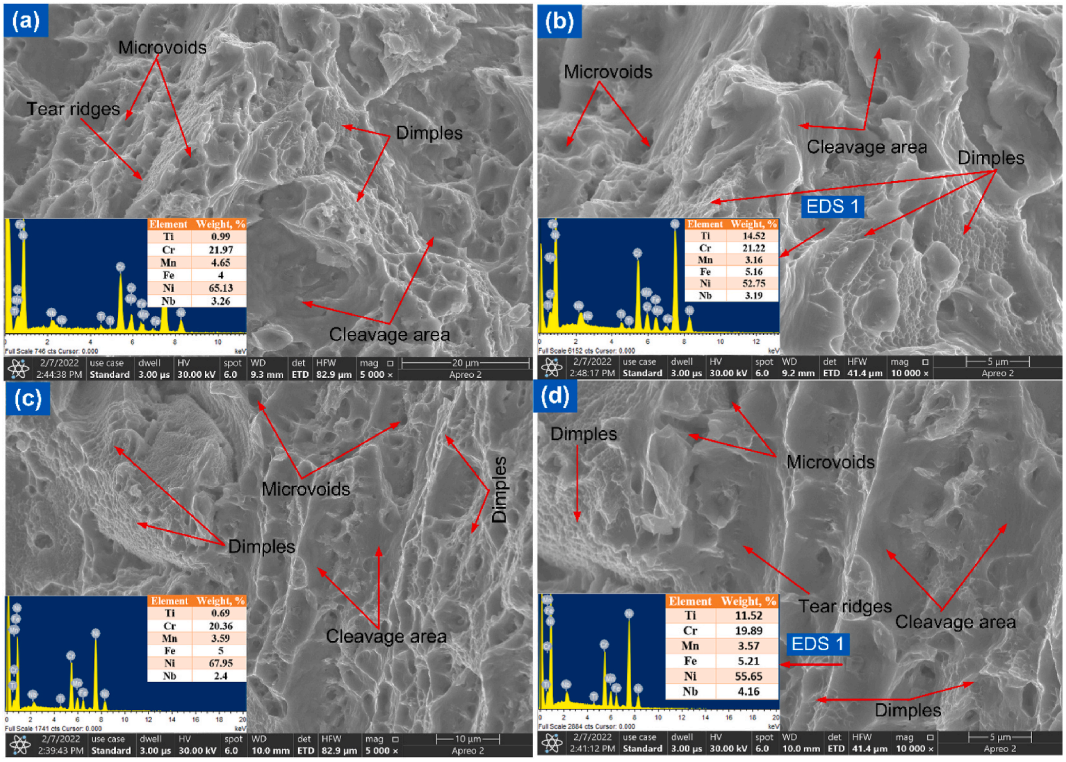

Fig. 25. Fractured surface of tensile tested specimen for VG weld joint in (a, b) AW state, (c, d) PWHT state.

The weld metal corresponding to the capping pass also shows a significant increase in hardness. The increase in hardness of the weld metal is attributed to an increase in the density of NbC and TiC particles in the inter-dendritic region. However, a significant effect of the PWHT was seen on the hardness of the P92 HAZ. The average hardness of the CGHAZ was 295 HV after PWHT which was reduced by approximately 34%. Similarly, the hardness of the FGHAZ also reduced from 414 ± 38 HV to 240 ± 7 HV. The ICHAZ shows the minute change in hardness and it was 225 HV after the PWHT. The average hardness at the interface of P92 BM was 240 ± 2 HV. The interface of IN617 BM and ERNiCr-3 weld metal also shows the hardness increase and it was 221 ± 7 HV after PWHT. A drastic increase in hardness of IN617 HAZ was observed and it was 210 ± 3 HV in AW and 260 ± 3 in the PWHT state. The drastic increment might be due to the evolution of secondary-phase carbide particles. The hardness indent for each region after the PWHT is given in Fig. 29b.

Effect of the welding passes on hardness variation for NVG joint in AW and PWHT stated in Fig. 30. Like VG welds joint, hardness variation across weldments corresponding to each pass is also measured for NVG welds joint. For NVG welds joint, a hardness trend along with the weld metal for different welding passes is also captured and presented in Fig. 30. A similar trend with a small deviation in hardness value was measured for the different welding passes. The average hardness of the ERNiCr-3 weld metal was measured as 221 ± 4 HV and 216 ± 8 HV for the filling passes at two different locations as mentioned in Fig. 30 (a, b). The average hardness of the weld metal corresponding to capping and the backing pass was 207 ± 5 HV (Figs. 30c) and 241 ± 8 HV (Fig. 30d). For the NVG welds joint, A similar trend of hardness variation along the weldments was measured as seen in the VG welds joint. However, the hardness of weld metal for NVG joint was measured much higher than the conventional VG. The hardness indent after the PWHT is depicted in Fig. 29. The hardness of IN617 HAZ, P92 CGHAZ, P92 FGHAZ, and P92 ICHAZ was 220 ± 2 HV, 427 HV, 412 ± 44, and 210 HV, respectively. A minute drop in the hardness value of CGHAZ and ICHAZ was measured as compared to the VG welds joint while an increase of 10 HV was seen in the hardness value of IN617 HAZ. The interface of ERNiCr-3 weld metal with P92 BM and IN617 BM shows the hardness of 235 ± 25 HV and 231 ± 4 HV, respectively.

The PWHT effect on hardness variation is given in Fig. 30(a–d). The average hardness for the filling pass at two different locations was 207 ± 4 HV (Figs. 30a) and 195 ± 7 HV (Fig. 30b) and that was similar to the VG welds joint. It shows a significant decrease, i.e. from 221 ± 4 HV to 207 ± 4 HV at location 1 (Figs. 30a) and 216 ± 8 HV to 195 ± 7 HV at location (Fig. 30b). The average hardness of the weld metal for the capping pass (Fig. 28c) and backing pass (Fig. 30d) was 209 ± 8 HV and 204 ± 6 HV, respectively. The weld corresponding to the backing pass also shows a significant decrease in hardness and it was reduced from 241 ± 8 HV to 200 ± 6 HV. The HAZ corresponding to P92 steel shows a significant decrease in hardness which is similar to the VG welds joint. The hardness of each HAZ region is mentioned in Fig. 29. The average hardness at the interface of ERNiCr-3 weld metal and P92 BM was 219 ± 21 HV. The interface of IN617 BM and ERNiCr-3 weld metal shows the hardness increase and it was 242 ± 8 HV after PWHT. Similar to the VG weld joint, the hardness of the IN617 for the NVG weld joint also increased after the PWHT and it was measured as 263 ± 4 HV. After a detailed investigation, it can be stated that the average hardness of the weld metal, P92 FGHAZ, and IN617 HAZ remain almost

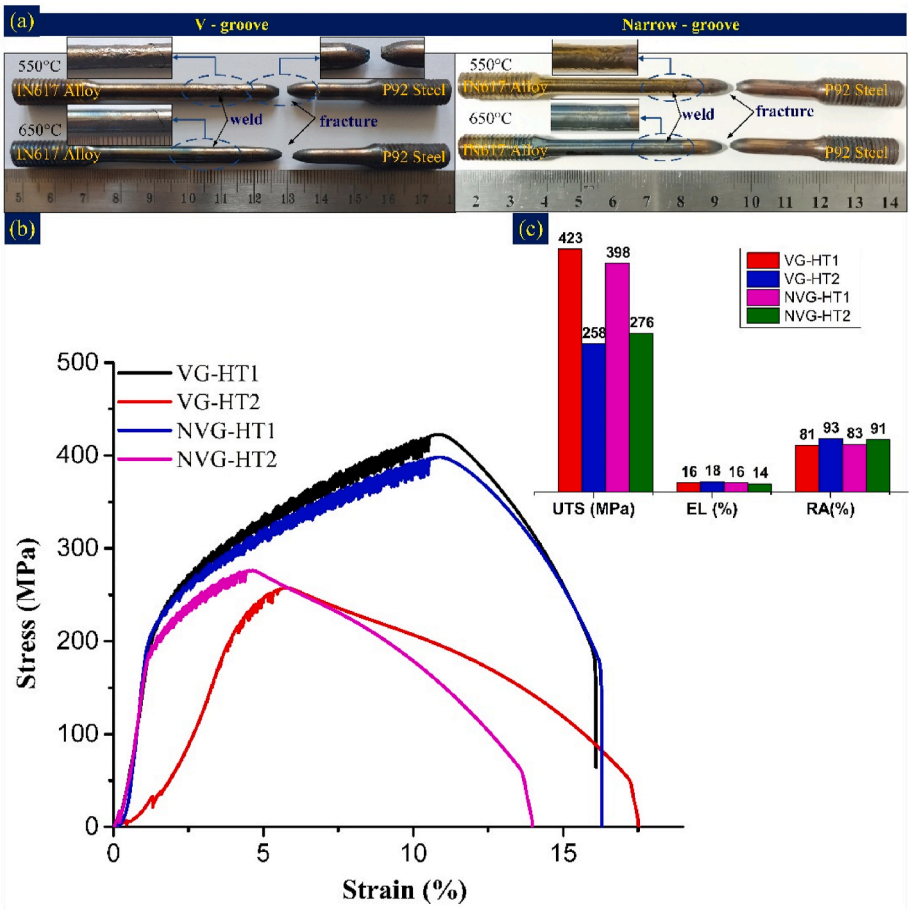

Fig. 26. (a) Tensile specimen after fracture, (b) stress-strain plot, (c) tensile properties.

constant. However, a significant effect of the groove geometry on the hardness of the interface region, P92 CGHAZ and P92 ICHAZ was observed. In weld metal, the maximum hardness was measured corresponding to the backing pass for both the groove joints in the AW condition that is attributed to the grain refinement effect as discussed by Zhang et al. [67]. A uniform hardness is also seen in a wide region of weld metal for capping and filling passes. In the capping pass, uniform hardness value might be due to the wide weld bead and less effect of the subsequent passes on microstructure evolution.

An impact test was performed for both the AW and PWHT condition and for both case notch in capping as well as in backing passes. The impact toughness for the VG joint was 177 J and 183 J for a sample having a notch in the root, i.e. backing pass, and in the top i.e. capping pass, respectively. As compared to the VG welds joint, the NVG welds joint offers poor impact toughness for both cases, i.e. notch in capping pass (169 J) and backing pass (161 J). However for both the groove design and notch location, welded joint meets the minimum criteria of 47 J [68]. The weld also meets the ASME standard (minimum required impact toughness of about 41 J). Hence, from impact test results it can be inferred that welded joint is qualified for AUSC boiler application in respect of impact toughness. Also, the impact toughness of the ERNiCr-3 fillet weld for both VG and NVG geometry exceeds the minimum suggested value of 80 J to qualify the fast breeder reactor application for dissimilar welded joints [69]. For a similar type of welded joint with BOHLER P92-IG filler, poor impact toughness of 36 J was measured due to the untempered martensitic microstructure [51]. However, for Ni-based IN617 filler, the impact toughness of VG welds joint was 98 J and 108 J for notch location in capping and backing pass, respectively. Naffakh et al. [70] also measured the higher impact toughness value for the IN82 filler than the IN617 filler.

After the PWHT, a little decrease in impact toughness was noticed for both types of groove joints and notch locations. For conventional VG, the impact toughness was 152 J and 157 J for the notch location in the backing and capping pass, respectively. In the NVG joint for notch location in capping and backing pass, impact toughness was 144 J and 164 J, respectively. The impact specimen showed a complete fracture in two parts for the VG joint (Fig. 31a). However, for the NVG joint, weld metal with a notch location in the capping pass showed the complete fracture while the sample with a notch location in the backing pass showed the yielding (Fig. 31b). Following the PWHT, higher density NbC and TiC particles along the inter-dendritic zones and boundaries which were also observed from the EDS results and shown in Fig. 32d, were primarily responsible for the loss in impact toughness. For BOHLER P92-IG filler, a drastic increase in impact toughness of the weld metal was reported after the PWHT [51] however for IN617 filler a similar behaviour was observed, i.e. decrease in impact toughness after PWHT [40]. The austenitic microstructure of the Ni-based filler does not

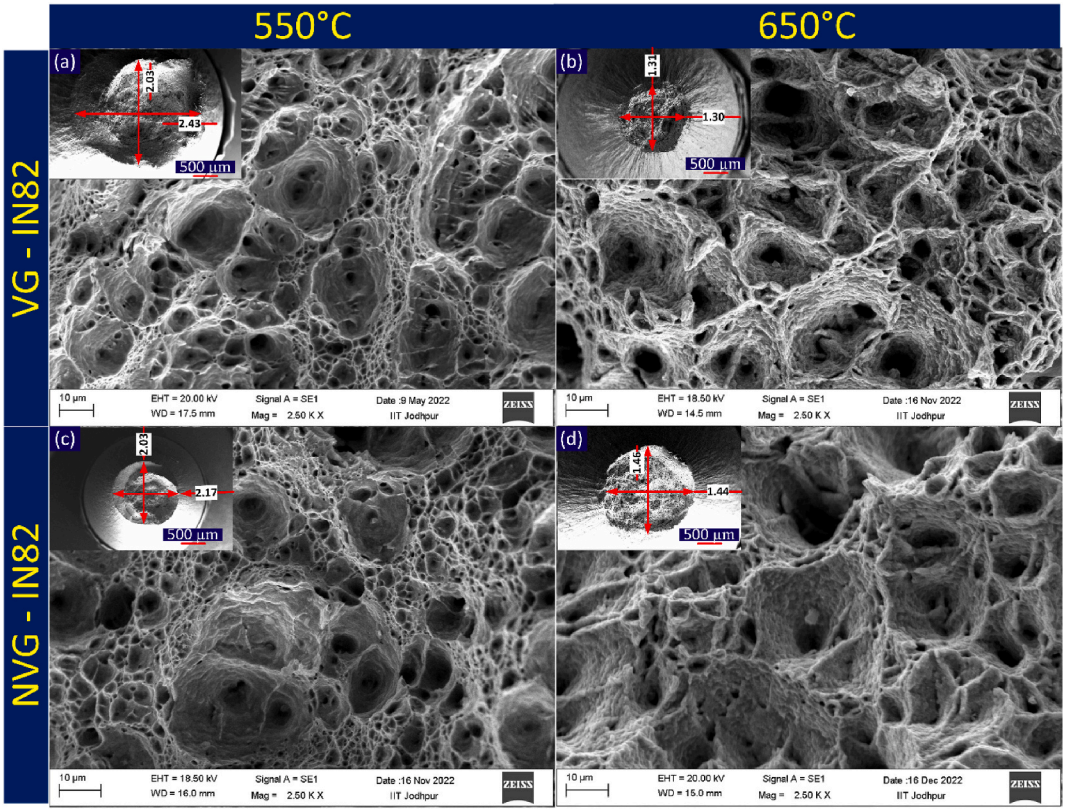

Fig. 27. A top and detailed view of the fracture surface (a) VG-HT1, (b) VG-HT2, (c) NVG-HT1, (d) NVG-HT2.

significantly alter throughout the PWHT, but there is a little increase in the density of the secondary phase particles, which reduces the weld metal's impact toughness.

The fractured impact tested specimen for the VG joint with a notch in the capping pass was characterized using FESEM and presented in Fig. 32. The fracture surface exhibited the shear dimples, microvoids, and cleavage area in both AW (Fig. 32a) and PWHT (Fig. 32c) conditions. The lower toughness of the weld metal (Fig. 31) could be attributed to the presence of Ti(C, N), NbC, and $M_{23}C_6$ carbide phase which was witnessed from EDS results presented in Fig. 32b-d. However, the AW impact-tested specimen showed a higher density of dimples than the PWHT-tested specimen (Fig. 32a, c). After PWHT, the density of the microvoids was increased as shown in Fig. 32c. The EDS of the selected area showed the presence of Ti, Cr, Mn, Fe, Ni, and Nb (Fig. 32b–d). The EDS of the particles showed the Cr, Ti, and Nb as major elements which confirmed the possible phase of $M_{23}C_6$, NbC, and Ti(C, N). Kumar et al. [71] have also observed the poor impact toughness of ERNiCr-3 filler weld for dissimilar metal weld of T91 and SS304H and NbC and TiC in weld metal were considered as the possible cause of poor impact toughness.

2.5.3. *Residual stresses*

Fig. 33 displays the residual stress map for the VG and NVG weld joints along the thickness of the welded plate. At a depth of 3 mm from the top surface, the peak longitudinal residual stress was measured to be 362 MPa for the VG and 290 MPa for the NVG welds joint. The minimum magnitude of longitudinal residual stresses of 198 MPa and 62 MPa were measured for VG and NVG welds joint, respectively. The minimum magnitude was in the root area of the welded joint. However, the trend of longitudinal residual stress variation was similar for both joints. The magnitude of the longitudinal residual stresses increases first from the top surface and reaches up to the highest point and then decreases for both VG and NVG welds joint. The nature of the longitudinal residual stresses was tensile from top to bottom and for both the grove joint. A similar trend with less magnitude was observed for transverse residual stresses. The peak magnitude was 315 MPa and 220 MPa for the VG and NVG welds joint, respectively and it was also measured at depth of 3 mm from the top surface. The minimum magnitude was 120 MPa and 10 MPa in the root area for the VG and NVG welds joint, respectively. The nature of the transverse residual was tensile from top to bottom surface in the VG welds joint (Fig. 33a) while it was compressive in the root area for the NVG welds joint (Fig. 33b). PWHT has resulted in a significant reduction in the magnitude of the residual stresses for both the weld groove designs (Fig. 33). After PWHT, the peak magnitude of the longitudinal residual stress is reduced by 41% in VG welds joint and by 57% in NVG welds joint. The nature of the longitudinal residual stress was tensile throughout the thickness for the VG welds joint while in the NVG welds joint it was compressive in the root area and the peak magnitude was 37 MPa. The transverse residual stress decreased by 38% and 47% for VG and NVG welds joint, respectively as a result of PWHT. The nature of the transverse residual stresses was compressive in the root area with a maximum magnitude of 68 MPa. In VG welds joint, the transverse residual

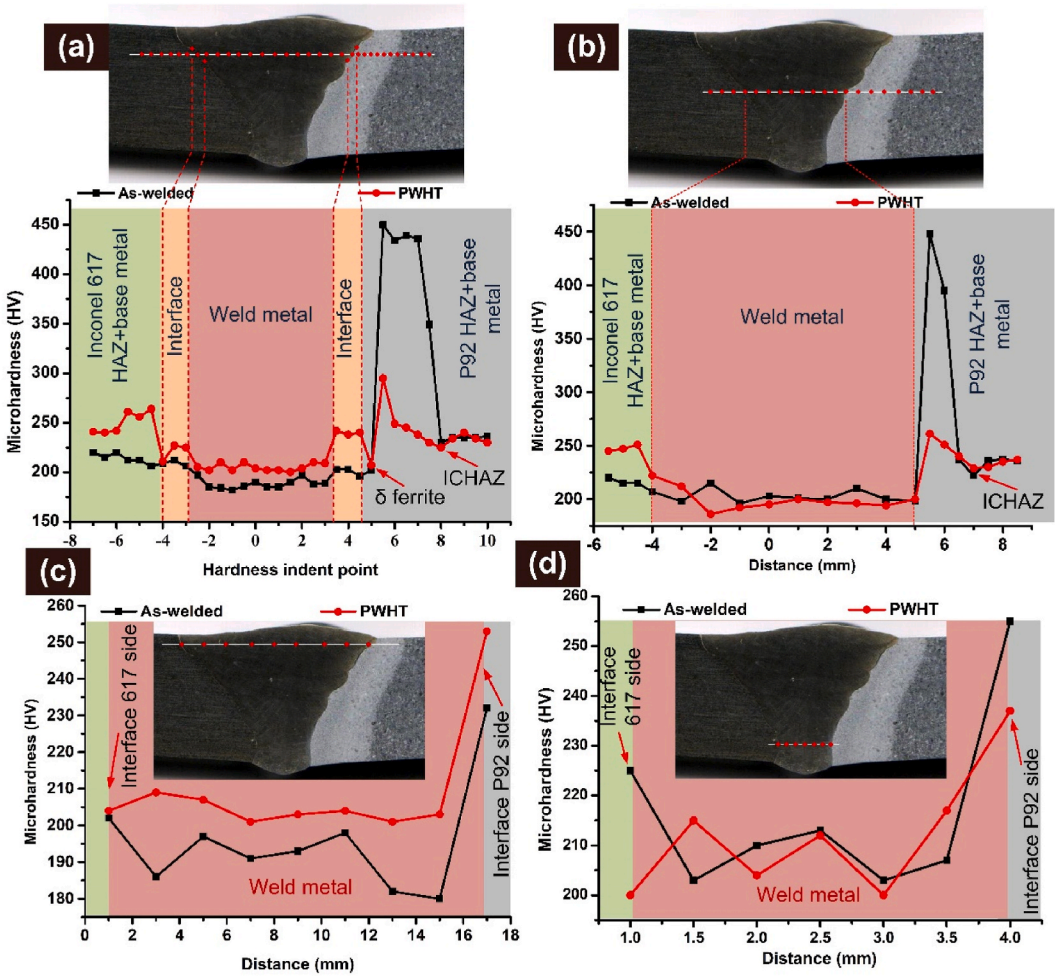

Fig. 28. (a, b, c and d) Hardness variation along the weldments corresponding to filling, backing, and capping pass for VG joint (AW and PWHT).

stress nature was tensile in the root area with a magnitude of 10 MPa (Fig. 33b).

3. Conclusions

The article content is focused on GTAW dissimilar welded joints characterization. Welded joints from 10 mm thick P92 steel and IN617 alloy produced with the use of ERNiCr-3 filler and different groove geometry were subjected to structural and mechanical investigations. The welding procedures made sound welded joints with four passes. No pores, undercuts and noticeable geometric shape imperfections were found, and the results show that produced welded joints are suitable for AUSC power plants' boiler applications. The conclusions summarized from the test results are as follows.

1. The tested welded joints have a complex and heterogeneous structure. The analysis of solidification mode and metallographic tests showed that the weld has a fully austenitic structure with 68.29 wt % of nickel and would not cause any solidification cracks. The ERNiCr-3 filler weld showed the equiaxed structure in the central region, while near to interface, columnar and cellular dendrites were seen. The EDS and EPMA study confirmed the presence of the Ti-rich Ti(C, N) and Nb-rich NbC particles in the weld metal.
2. The heterogeneity in the microstructure of the ERNiCr-3 filler weld was also seen mainly due to the multiple heating cycles. The migrated grain boundaries (MGBs) are seen higher in the number of weld metal corresponding to filling passes than capping and backing passes weld metal. The heterogeneity observed in the microstructure of the ERNiCr-3 filler weld metal was also attributed to the segregation of Nb particles in the inter-dendritic areas.
3. A fusion boundary of weld filler deficient zones was revealed, formed due to the large differences in physicochemical properties between ERNiCr-3 filler and P92 steel, in the shape of filler deficient beach, i.e. unmixed zone, peninsula, and island along with distinct HAZ. Another fusion boundary of the weld was revealed, at the interface of IN617 and ERNiCr-3 weld metal, in the form of a very narrow partial melted zone and almost negligible unmixed zone along with HAZ. The EDS and EPMA mapping

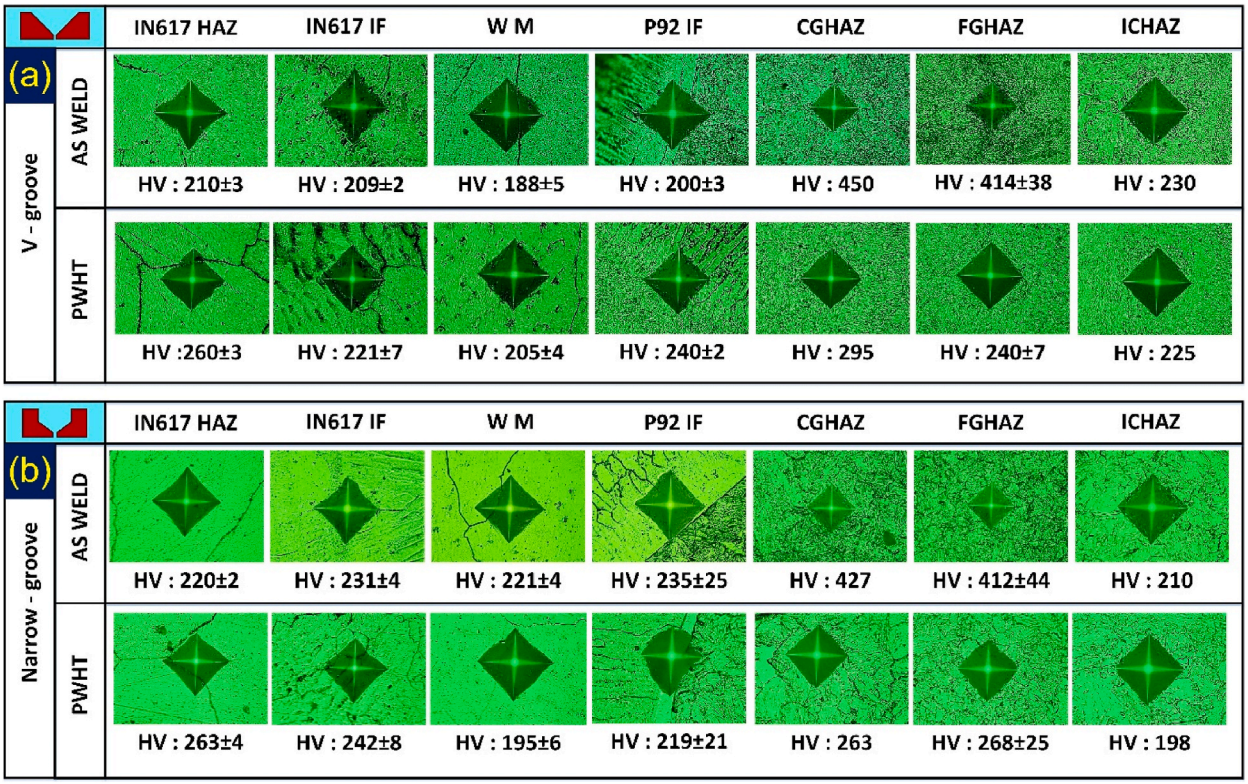

Fig. 29. Hardness indent along weldments of (a)VG and (b) NVG, for both AW and PWHT state.

conducted across the interface of P92 steel and ERNiCr-3 filler weld confirmed the diffusion of Ni and Cr from the filler weld into the P92 steel, as well as the diffusion of Fe from P92 steel into the filler weld. The compositional similarity between the filler and IN617 BM resulted in a negligible diffusion of elements observed at the interface on the IN617 side.

4. Tensile test results showed the failure of the specimens from the ERNiCr-3 filler weld for both the groove geometry and heat treatment condition. The weld groove geometry had observed a minute effect on tensile properties in as-welded conditions. The tensile strength of 627 $\pm$ 2 MPa for VG and 636 $\pm$ 3 MPa for NVG welds joint had been observed. The FESEM study of the fracture surface showed the presence of Ti(C, N) and NbC particles.
5. The tensile tests conducted at high temperatures of 550 °C and 650 °C revealed that both VG and NVG welds joints failed in the region of P92 BM. The tensile strengths for VG-HT1 and VG-HT2 were 423 MPa and 258 MPa, respectively. Similarly, the NVG-HT1 and NVG-HT2 exhibited tensile strengths of 398 MPa and 276 MPa, respectively.
6. The welding pass and segregation of the alloying elements like Nb have observed a significant effect on the hardness of the ERNiCr-3 filler weld. However, as compared to other zones of the weldments, the hardness of the ERNiCr-3 filler weld was found to have plummeted. The peak hardness was measured in P92 CGHAZ.
7. Observations revealed brittle Ti(C, N) and NbC particles present in the inter-dendritic space, which led to a decrease in the impact toughness of the weld metal in comparison to the base metal. Nevertheless, the impact toughness values for all cases met the criterion of 80 J, thus qualifying the dissimilar welded joint for use in fast breeder reactor applications. Moreover, the VG welded joint exhibited higher impact toughness measurements than the NVG welded joint.
8. The distributions of the values of longitudinal and transverse residual stress showed a similar trend for both variants of the geometry of welded joints: the maximum value of the magnitude of tensile residual stress occurred in the central area of the joints, and the minimum in the root area. Only in the case of the root of the NVG joint the nature of the transverse residual stresses was compressive.
9. For both variants of welded joints, PWHT caused similar effects: a significant increase in the tensile strength of VG welded joints and a small increase in the tensile strength of NVG welded joints, a very large drop in the maximum hardness of HAZ (at ERNiCr-3 and P92 steel side), a small decrease in impact toughness of the weld metal, a significant reduction in the magnitude of the residual stress, and the more uniform distribution of the NbC and TiC precipitates in comparison with the AW joints. It was also found that PWHT had a negligible effect on the austenitic microstructure of ERNiCr-3 filler weld and IN617 HAZ.
10. Based on the comprehensive study conducted on dissimilar IN617 and P92 steel weldments, it can be concluded that NVG joints exhibit superior mechanical properties and lower residual stress values when compared to conventional VG joints. Considering the similar structural morphology of both types of joints, it is recommended that the NVG procedure be implemented in the power industry.

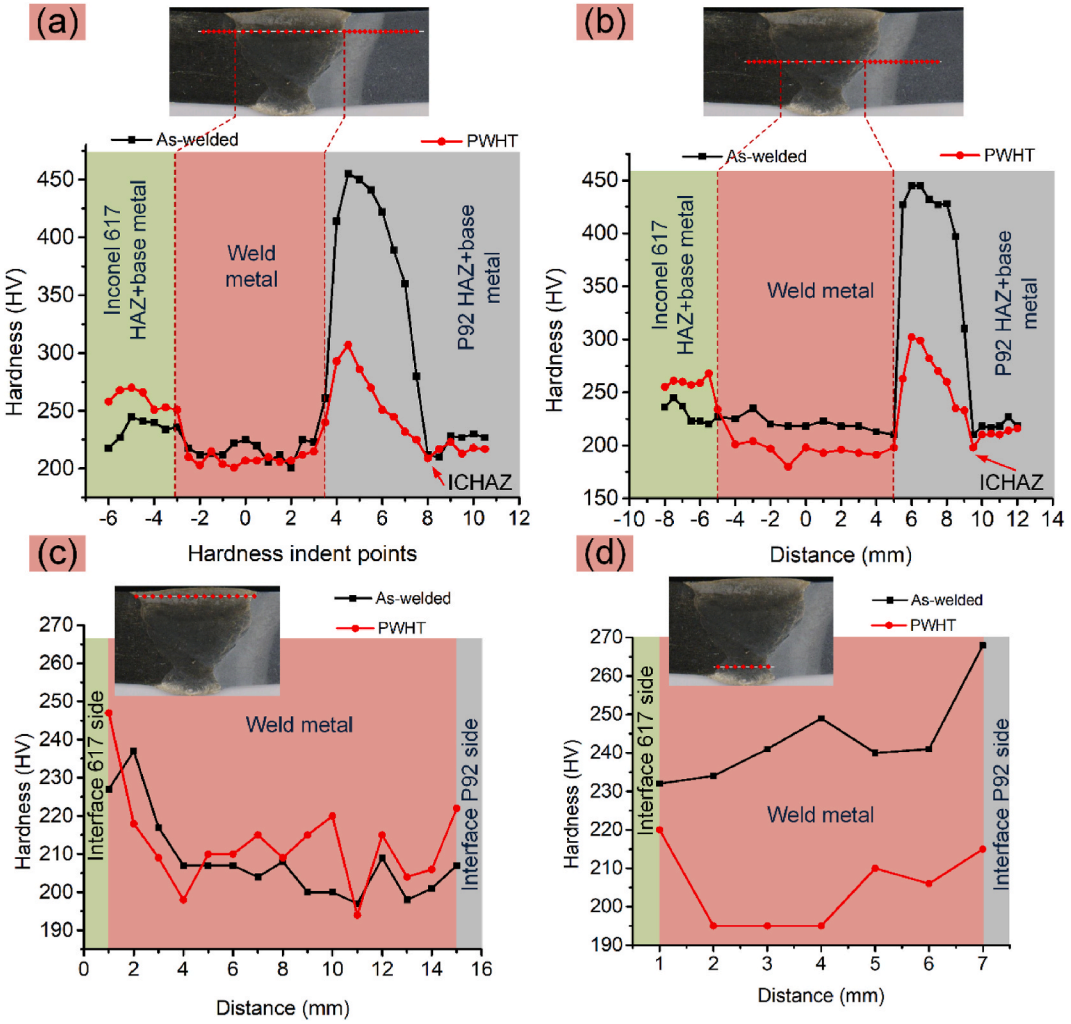

Fig. 30. (a, b, c and d) Hardness variation for NVG joint in AW and PWHT state.

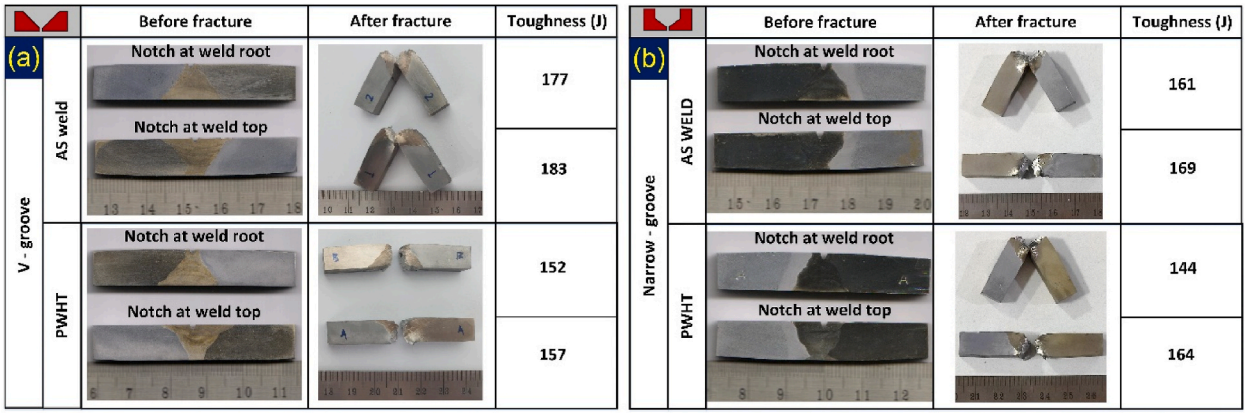

Fig. 31. Impact toughness test results of (a)VG and (b) NVG for AW and PWHT states.

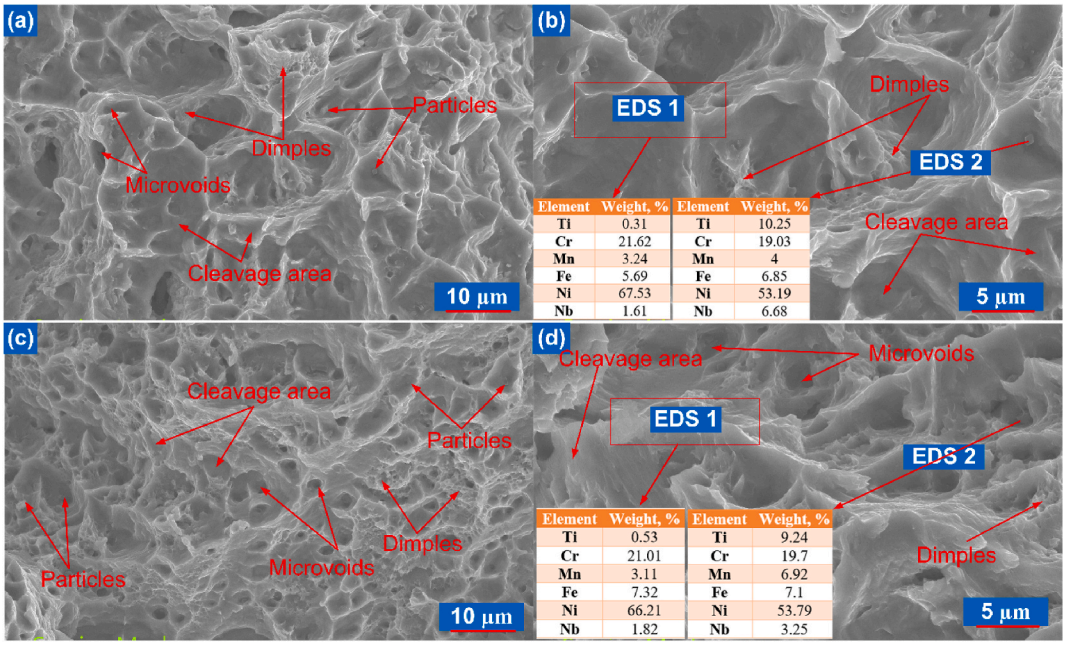

Fig. 32. FESEM image of fractured impact tested specimen for VG welded joints with a notch in capping pass; (a, b) AW, (c, d) PWHT.

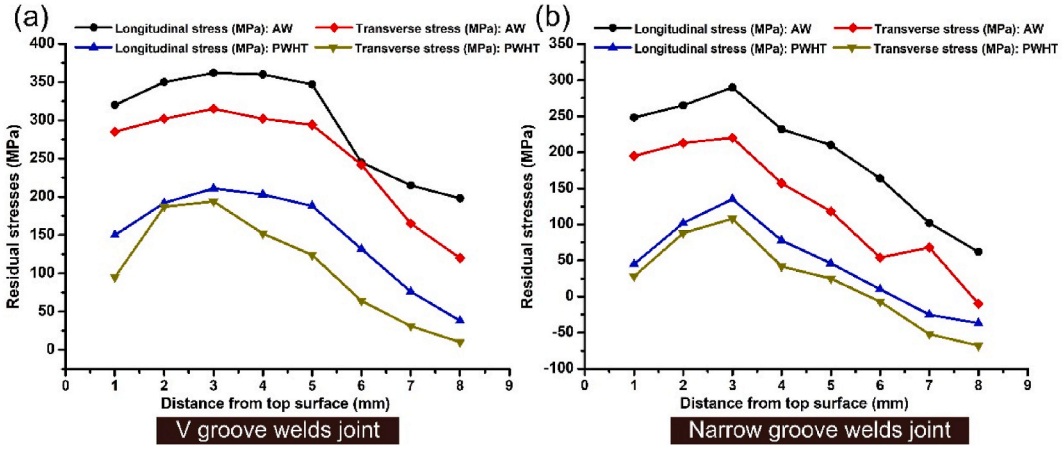

Fig. 33. Residual stresses distribution in ERNiCr-3 filler weld along with thickness for (a) VG welds joint, (b) NVG welds joint.

Author contribution statement

Amit Kumar: Conceived and designed the experiments; Performed the experiments; Analyzed and interpreted the data; Wrote the paper. Shailesh M Pandey, Sachin Sirohi: Conceived and designed the experiments; Performed the experiments; Wrote the paper. D. Fydrych, C. Pandey: Conceived and designed the experiments; Performed the experiments; Analyzed and interpreted the data; Contributed reagents, materials, analysis tools or data.

Funding statement

This research did not receive any specific grant from funding agencies in the public, commercial, or not-for-profit sectors.

Data availability statement

Data will be made available on request.

Declaration of competing interest

The authors declare that they have no known competing financial interests or personal relationships that could have appeared to influence the work reported in this paper.

Acknowledgments

The authors would like to thank Indian Institute of Technology Jodhpur, India, for providing funding to the research project entitled “Study on weldability issues, diffusible hydrogen, and residual stresses in dissimilar welds joint of Ni-based super alloy (IN617) and ferritic/martensitic grade P92 steel” under the Grant No. SEED/CHP/20210130.

References

[1] R. Kumar, H.C. Dey, A.K. Pradhan, M.M. Mahapatra, C. Pandey, Residual stresses study in butt welded joint of Inconel 617 alloy and effect of post weld heat treatment on residual stresses, Proc. Inst. Mech. Eng. Part L J. Mater. Des. Appl. (2023), 146442072211492, https://doi.org/10.1177/14644207221149205.
[2] J.H. Lee, J.H. Hwang, Y.S. Park, T.M. Kim, D.H. Bae, W.B. Seo, J.W. Han, Assessing mechanical properties of the dissimilar metal welding between P92 steels and alloy 617 at high temperature, J. Mech. Sci. Technol. 30 (2016) 4453–4457, https://doi.org/10.1007/s12206-016-0911-1.
[3] F. Abe, Research and development of heat-resistant materials for advanced USC power plants with steam temperatures of 700 °C and above, Engineering 1 (2015) 211–224, https://doi.org/10.15302/J-ENG-2015031.
[4] W. Jamrozik, M. Kiel-jamrozik, Heliyon the effect of TIG welding on the structure and hardness of butt joints made of, Inconel 718 (2023) 9, https://doi.org/10.1016/j.heliyon.2023.e13175.
[5] J. Akram, P.R. Kalvala, M. Misra, I. Charit, Creep behavior of dissimilar metal weld joints between P91 and AISI 304, Mater. Sci. Eng. 688 (2017) 396–406, https://doi.org/10.1016/j.msea.2017.02.026.
[6] S. Sirohi, A. Kumar, S. Soni, G. Dak, S. Kumar, A. Świerczyńska, G. Rogalski, D. Fydrych, C. Pandey, Influence of PWHT parameters on the mechanical properties and microstructural behavior of multi-pass GTAW joints of P92 steel, Materials 15 (2022) 4045, https://doi.org/10.3390/ma15124045.
[7] R.L. Klueh, D.R. Harries, High-Chromium Ferritic and Martensitic Steels for Nuclear Applications, ASTM, 2001, https://doi.org/10.1520/mono3-eb.
[8] C. Pandey, M.M. Mahapatra, P. Kumar, Effect of post weld heat treatments on fracture frontier and type IV cracking nature of the crept P91 welded sample, Mater. Sci. Eng. 731 (2018) 249–265, https://doi.org/10.1016/j.msea.2018.06.038.
[9] Y. Zhang, K. Li, Z. Cai, J. Pan, Creep rupture properties of dissimilar metal weld between Inconel 617B and modified 9%Cr martensitic steel, Mater. Sci. Eng. 764 (2019), 138185, https://doi.org/10.1016/j.msea.2019.138185.
[10] G. Dak, S.M. Pandey, C. Pandey, Residual stress analysis, microstructural characterization, and mechanical properties of tungsten inert gas-welded P92/AISI 304L dissimilar steel joints, Proc. Inst. Mech. Eng. Part L J. Mater. Des. Appl. 237 (2023) 767–790, https://doi.org/10.1177/14644207221124494.
[11] S. Sirohi, C. Pandey, A. Goyal, Role of the Ni-based filler (IN625) and heat-treatment on the mechanical performance of the GTA welded dissimilar joint of P91 and SS304H steel, J. Manuf. Process. 65 (2021) 174–189, https://doi.org/10.1016/j.jmapro.2021.03.029.
[12] H. Shah Hosseini, M. Shamanian, A. Kermanpur, Characterization of microstructures and mechanical properties of Inconel 617/310 stainless steel dissimilar welds, Mater. Char. 62 (2011) 425–431, https://doi.org/10.1016/j.matchar.2011.02.003.
[13] A. Celik, A. Alsaran, Mechanical and structural properties of similar and dissimilar steel joints, Mater. Char. 43 (1999) 311–318, https://doi.org/10.1016/S1044-5803(99)00045-5.
[14] C.D. Lundin, Dissimilar metal welds-transition joints literature review, Weld. J. (1982) 58s–63s.
[15] G. Dak, N. Khanna, C. Pandey, Study on narrow gap welding of martensitic grade P92 and austenitic grade AISI 304L SS steel for ultra-supercritical power plant application, Arch. Civ. Mech. Eng. 23 (2023) 14, https://doi.org/10.1007/s43452-022-00540-3.
[16] X. Xing, X. Di, B. Wang, The effect of post-weld heat treatment temperature on the microstructure of Inconel 625 deposited metal, J. Alloys Compd. 593 (2014) 110–116, https://doi.org/10.1016/j.jallcom.2013.12.224.
[17] R. Mittal, B.S. Sidhu, Microstructures and mechanical properties of dissimilar T91/347H steel weldments, J. Mater. Process. Technol. 220 (2015) 76–86, https://doi.org/10.1016/j.jmatprotec.2015.01.008.
[18] K.D. Ramkumar, P.S.G. Kumar, V.R. Krishna, A. Chandrasekhar, S. Dev, W.S. Abraham, S. Prabhakaran, S. Kalainathan, R. Sridhar, Influence of laser peening on the tensile strength and impact toughness of dissimilar welds of Inconel 625 and UNS S32205, Mater. Sci. Eng. 676 (2016) 88–99, https://doi.org/10.1016/j.msea.2016.08.104.
[19] K.R. Vishwakarma, N.L. Richards, M.C. Chaturvedi, Haz microfissuring in EB welded allvac 718 plus™ alloy, Proc. Int. Symp. Superalloys Var. Deriv. (2005) 637–647, https://doi.org/10.7449/2005/superalloys_2005_637_647.
[20] S.L. Jeng, H. Ten Lee, T.Y. Kuo, K.C. Tsai, C.L. Chung, J.Y. Huang, The effects of Mn and Nb on the microstructure and mechanical properties of Alloy 152 welds, Mater. Des. 87 (2015) 920–931, https://doi.org/10.1016/j.matdes.2015.08.100.
[21] O.A. Ojo, N.L. Richards, M.C. Chaturvedi, Microstructural study of weld fusion zone of TIG welded IN 738LC nickel-based superalloy, Scripta Mater. 51 (2004) 683–688, https://doi.org/10.1016/j.scriptamat.2004.06.013.
[22] M. Sireesha, V. Shankar, S.K. Albert, S. Sundaresan, Microstructural features of dissimilar welds between 316LN austenitic stainless steel and alloy 800, Mater. Sci. Eng. 292 (2000) 74–82, https://doi.org/10.1016/S0921-5093(00)00969-2.
[23] A.H.V. Pavan, K.S.N. Vikrant, R. Ravibharath, K. Singh, Development and evaluation of SUS 304H — IN 617 welds for advanced ultra supercritical boiler applications, Mater. Sci. Eng. 642 (2015) 32–41, https://doi.org/10.1016/j.msea.2015.06.065.
[24] Y. Zhang, H. Jing, L. Xu, Y. Han, L. Zhao, B. Xiao, Microstructure and mechanical performance of welded joint between a novel heat-resistant steel and Inconel 617 weld metal, Mater. Char. 139 (2018) 279–292, https://doi.org/10.1016/j.matchar.2018.03.012.
[25] A. Kumar, C. Pandey, Autogenous laser-welded dissimilar joint of ferritic/martensitic P92 steel and Inconel 617 alloy: mechanism, microstructure, and mechanical properties, Arch. Civ. Mech. Eng. 22 (2022) 39, https://doi.org/10.1007/s43452-021-00365-6.
[26] H. Naffakh, M. Shamanian, F. Ashrafizadeh, Microstructural evolutions in dissimilar welds between AISI 310 austenitic stainless steel and Inconel 657, J. Mater. Sci. 45 (2010) 2564–2573, https://doi.org/10.1007/s10853-010-4227-8.
[27] K. Ding, P. Wang, X. Liu, X. Li, B. Zhao, Y. Gao, Formation of lamellar carbides in alloy 617-HAZ and their role in the impact toughness of alloy 617/9%Cr dissimilar welded joint, J. Mater. Eng. Perform. 27 (2018) 6027–6039, https://doi.org/10.1007/s11665-018-3668-0.
[28] C. Pandey, M.M. Mahapatra, P. Kumar, Fracture behaviour of crept P91 welded sample for different post weld heat treatments condition, Eng. Fail. Anal. (2018), https://doi.org/10.1016/j.engfailanal.2018.08.029.
[29] K.Y. Shin, J.W. Lee, J.M. Han, K.W. Lee, B.O. Kong, H.U. Hong, Transition of creep damage region in dissimilar welds between Inconel 740H Ni-based superalloy and P92 ferritic/martensitic steel, Mater. Char. 139 (2018) 144–152, https://doi.org/10.1016/j.matchar.2018.02.039.
[30] G. Wu, K. Ding, T. Wei, S. Qiao, X. Liu, Y. Gao, Rupture behavior and fracture mode for Inconel 625–9% Cr steel dissimilar welded joints at high temperature, Eng. Fail. Anal. 125 (2021), 105412, https://doi.org/10.1016/j.engfailanal.2021.105412.
[31] P.K. Taraphdar, R. Kumar, A. Giri, C. Pandey, M.M. Mahapatra, K. Sridhar, Residual stress distribution in thick double-V butt welds with varying groove configuration , restraints and mechanical tensioning, J. Manuf. Process. 68 (2021) 1405–1417, https://doi.org/10.1016/j.jmapro.2021.06.046.
[32] J. Lee, J. Hwang, D. Bae, Welding residual stress analysis and fatigue strength assessment at elevated temperature for multi-pass dissimilar material weld between alloy 617 and P92 steel, Met. Mater. Int. 24 (2018) 877–885, https://doi.org/10.1007/s12540-018-0086-7.

[33] G. Dak, C. Pandey, Experimental investigation on microstructure, mechanical properties, and residual stresses of dissimilar welded joint of martensitic P92 and AISI 304L austenitic stainless steel, Int. J. Pres. Ves. Pip. 194 (2021), 104536, https://doi.org/10.1016/j.ijpvp.2021.104536.

[34] W. Yan, W. Wang, Y.Y. Shan, K. Yang, Microstructural stability of 9-12%Cr ferrite/martensite heat-resistant steels, Front. Mater. Sci. 7 (2013) 1–27, https://doi.org/10.1007/s11706-013-0189-5.

[35] A. Kumar, C. Pandey, Development and evaluation of dissimilar gas Tungsten Arc-welded joint of P92 steel/inconel 617 alloy for advanced ultra-supercritical boiler applications, Metall. Mater. Trans. 53 (2022) 3245–3273, https://doi.org/10.1007/s11661-022-06723-0.

[36] M. Akbari-Garakani, M. Mehdizadeh, Effect of long-term service exposure on microstructure and mechanical properties of Alloy 617, Mater. Des. 32 (2011) 2695–2700, https://doi.org/10.1016/j.matdes.2011.01.017.

[37] A. Kumar, C. Pandey, Structural integrity assessment of Inconel 617/P92 steel dissimilar welds for different groove geometry, Sci. Rep. (2023) 1–29, https://doi.org/10.1038/s41598-023-35136-1.

[38] W. Ren, F. Lu, R. Yang, X. Liu, Z. Li, Liquation cracking in fiber laser welded joints of inconel 617, J. Mater. Process. Technol. 226 (2015) 214–220, https://doi.org/10.1016/j.jmatprotec.2015.07.004.

[39] W. Ren, F. Lu, P. Nie, R. Yang, X. Liu, K. Feng, Z. Li, Effects of the long-time thermal exposure on the microstructure and mechanical properties of laser weldings of Inconel 617, J. Mater. Process. Technol. 247 (2017) 296–305, https://doi.org/10.1016/j.jmatprotec.2017.05.003.

[40] A. Kumar, C. Pandey, Development and evaluation of dissimilar gas Tungsten Arc-welded joint of P92 steel/inconel 617 alloy for advanced ultra-supercritical boiler applications, Metall. Mater. Trans. 53 (2022) 3245–3273, https://doi.org/10.1007/s11661-022-06723-0.

[41] A. Kumar, C. Pandey, Some studies on dissimilar welds joint P92 steel and Inconel 617 alloy for AUSC power plant application, Int. J. Pres. Ves. Pip. 198 (2022), 104678, https://doi.org/10.1016/j.ijpvp.2022.104678.

[42] C. Pandey, A. Giri, M.M. Mahapatra, On the prediction of effect of direction of welding on bead geometry and residual deformation of double-sided fillet welds, Int. J. Steel Struct. 16 (2016) 333–345, https://doi.org/10.1007/s13296-016-6007-z.

[43] N. Sayyar, M. Shamanian, B. Niroumand, J. Kangazian, J.A. Szpunar, EBSD observations of microstructural features and mechanical assessment of INCOLOY 825 alloy/AISI 321 stainless steel dissimilar welds, J. Manuf. Process. 60 (2020) 86–95, https://doi.org/10.1016/j.jmapro.2020.10.042.

[44] E.8 Astm, ASTM E8/E8M standard test methods for tension testing of metallic materials 1, Annu. Book ASTM Stand. 4 (2010) 1–27, https://doi.org/10.1520/E0008.

[45] A. E23-02a, ASTM E23-02a - Notched Bar Impact Testing of Metallic Materials . Pdf, ASTM Int., 2002.

[46] P.K. Taraphdar, R. Kumar, C. Pandey, M.M. Mahapatra, Significance of finite element models and solid-state phase transformation on the evaluation of weld induced residual stresses, Met. Mater. Int. (2021), https://doi.org/10.1007/s12540-020-00921-4.

[47] J.N. Dupont, S.W. Banovic, A.R. Marder, Microstructural evolution and weldability of dissimilar welds between a super austenitic stainless steel and nickel-based alloys, Weld. J. 82 (2003) 125–135.

[48] H.T. Lee, S.L. Jeng, C.H. Yen, T.Y. Kuo, Dissimilar welding of nickel-based Alloy 690 to SUS 304L with Ti addition, J. Nucl. Mater. 335 (2004) 59–69, https://doi.org/10.1016/j.jnucmat.2004.06.004.

[49] J.C. Lippold, D.J. Kotecki, Welding Metallurgy and Weldability of Stainless Steels, John Wiley, 2005.

[50] S. Kumar, C. Pandey, A. Goyal, Effect of post-weld heat treatment and dissimilar filler metal composition on the microstructural developments, and mechanical properties of gas tungsten arc welded joint of P91 steel, Int. J. Pres. Ves. Pip. 191 (2021), 104373, https://doi.org/10.1016/j.ijpvp.2021.104373.

[51] A. Kumar, C. Pandey, Some studies on dissimilar welds joint P92 steel and Inconel 617 alloy for AUSC power plant application, Int. J. Pres. Ves. Pip. 198 (2022), 104678, https://doi.org/10.1016/j.ijpvp.2022.104678.

[52] S. Rahman, G. Priyadarshan, K.S. Raja, C. Nesbitt, M. Misra, Investigation of the secondary phases of alloy 617 by scanning kelvin probe force microscope, Mater. Lett. 62 (2008) 2263–2266, https://doi.org/10.1016/j.matlet.2007.11.077.

[53] H.S. Hosseini, M. Alishahi, M. Shamanian, Zonular evaluation of Inconel 617/310 SS dissimilar joint by shear punch test, Mater. Lett. 67 (2012) 259–262, https://doi.org/10.1016/j.matlet.2011.09.066.

[54] A. Kumar, S.M. Pandey, C. Pandey, Dissimilar Weldments of Ferritic/martensitic Grade P92 Steel and Inconel 617 Alloy: Role of Groove Geometry on Mechanical Properties and Residual Stresses, Springer London, 2023, https://doi.org/10.1007/s43452-022-00592-5.

[55] M. Jula, R. Dehmolaei, S.R. Alavi Zaree, The comparative evaluation of AISI 316/A387-Gr.91 steels dissimilar weld metal produced by CCGTAW and PCGTAW processes, J. Manuf. Process. 36 (2018) 272–280, https://doi.org/10.1016/j.jmapro.2018.10.032.

[56] H. Xu, M.J. Xu, C. Yu, H. Lu, X. Wei, J.M. Chen, J.J. Xu, Effect of the microstructure in unmixed zone on corrosion behavior of 439 tube/308L tube-sheet welding joint, J. Mater. Process. Technol. 240 (2017) 162–167, https://doi.org/10.1016/j.jmatprotec.2016.09.017.

[57] W.F. Savage, E.F. Nippes, E.S. Szekeres, Study of Weld Interface Phenomena in a Low Alloy Steel., Weld. J. (Miami, Fla, 1976, p. 55.

[58] Y.K. Yang, S. Kou, Mechanisms of Macrosegregation Formation Near Fusion Boundary in Welds Made with Dissimilar Filler Metals, 2007.

[59] C. Pan, Z. Zhang, Characteristics of the weld interface in dissimilar austentic-pearlitic steel welds, Mater. Char. 33 (1994) 87–92, https://doi.org/10.1016/1044-5803(94)90070-1.

[60] T.Y. Kuo, H.T. Lee, Effects of filler metal composition on joining properties of alloy 690 weldments, Mater. Sci. Eng. 338 (2002) 202–212, https://doi.org/10.1016/S0921-5093(02)00063-1.

[61] S. Kou, Welding Metallurgy, second ed., John Wiley Sons Publ, 2000, pp. 97–117.

[62] A.R.M.J.N. Dupont, C.V. Robino, Solidification modeling of Nb bearing superalloys, Weld. J. 77 (1998) 417.

[63] H. Shah Hosseini, M. Shamanian, A. Kermanpur, Microstructural and weldability analysis of Inconel617/AISI 310 stainless steel dissimilar welds, Int. J. Pres. Ves. Pip. 144 (2016) 18–24, https://doi.org/10.1016/j.ijpvp.2016.05.004.

[64] M. Sireesha, S.K. Albert, V. Shankar, S. Sundaresan, Comparative evaluation of welding consumables for dissimilar welds between 316LN austenitic stainless steel and Alloy 800, J. Nucl. Mater. 279 (2000) 65–76, https://doi.org/10.1016/S0022-3115(99)00275-5.

[65] H.Y. Han, Z. Sun, Welding of tube-to-tube joints between martensitic and austenitic stainless steels for reactor applications, Int. J. Pres. Ves. Pip. 60 (1994) 59–64, https://doi.org/10.1016/0308-0161(94)90113-9.

[66] R. Sridhar, K. Devendranath Ramkumar, N. Arivazhagan, Characterization of microstructure, strength, and toughness of dissimilar weldments of inconel 625 and duplex stainless steel SAF 2205, Acta Metall. Sin. (English Lett. 27 (2014) 1018–1030, https://doi.org/10.1007/s40195-014-0116-5.

[67] G. Dak, S. Sirohi, C. Pandey, Study on microstructure and mechanical behavior relationship for laser-welded dissimilar joint of P92 martensitic and 304L austenitic steel, Int. J. Pres. Ves. Pip. 196 (2022), 104629, https://doi.org/10.1016/j.ijpvp.2022.104629.

[68] S. Standard, Welding consumables - covered electrodes for manual metal arc welding of creep- resisting steels - classification (ISO 3580:2004), Com, Eur. Norm. 1999 (2008).

[69] PFBR/33700/SP/1008/R-0, Prototype Fast Breeder Specification for the Qualification of the Joint between 316LN Austenitic Stainless Steel and Alloy 800 as Proposed by IGCAR, Kalpakkam, India, ((n.d.)).

[70] H. Naffakh, M. Shamanian, F. Ashrafizadeh, Dissimilar welding of AISI 310 austenitic stainless steel to nickel-based alloy Inconel 657, J. Mater. Process. Technol. 209 (2009) 3628–3639, https://doi.org/10.1016/j.jmatprotec.2008.08.019.

[71] R. Kumar, A. Varma, Y.R. Kumar, S. Neelakantan, J. Jain, Enhancement of mechanical properties through modified post-weld heat treatment processes of T91 and Super304H dissimilar welded joint, J. Manuf. Process. 78 (2022) 59–70, https://doi.org/10.1016/j.jmapro.2022.04.008.